Supplementary Information

Cationic carbon nanotube modulates surface fields for general acidic CO_2 reduction with aqueous organic cations

Qiang Zhang[1,2#], Soonho Kwon[3,4#], Yan Guo[5], Tanglue Feng[6], Jianjun Su[1,2], Yun Song[1,2], Weihua Guo[1,2], Yinger Xin[1,2], Geng Li[1,2], Yong Liu[1,2], Mingming He[1,2], Rui Xue[1,2], Ruixuan Wang[1,2], Honglu Hu[2,7], Zhiyuan Zeng[2,7], Yongfa Zhu[8], Ben Zhong Tang[9,10], William A. Goddard III[3*] and Ruquan Ye[1,2*]

[1]Department of Chemistry, State Key Laboratory of Marine Environmental Health, City University of Hong Kong, Hong Kong 999077, P. R. China

[2]City University of Hong Kong Shenzhen Research Institute, Shenzhen, Guangdong 518057, P. R. China

[3]Materials and Process Simulation Center, California Institute of Technology, Pasadena 91125, California, United States

[4]Department of Materials Science and Engineering, Pohang University of Science and Technology (POSTECH), Pohang 37673, R. Korea

[5]Department of Civil Engineering, The University of Hong Kong, Hong Kong 999077, P. R. China

[6]School of Chemical Engineering, Zhengzhou University, Zhengzhou 450001, P. R. China

[7]Department of Materials Science and Engineering, State Key Laboratory of Marine Pollution, City University of Hong Kong, Hong Kong 999077, P. R. China

[8]Department of Chemistry, Tsinghua University, Beijing 100084, P. R. China

[9]School of Science and Engineering, Shenzhen Institute of Aggregate Science and Technology, The Chinese University of Hong Kong, Shenzhen (CUHK-Shenzhen), Guangdong 518172, P. R. China

[10]Department of Chemistry and the Hong Kong Branch of Chinese National Engineering Research Center for Tissue Restoration and Reconstruction, The Hong Kong University of Science and Technology, Hong Kong 999077, P. R. China

[#]Equal contribution

[*]Corresponding authors:

William A. Goddard III: wag@caltech.edu; ORCID:0000-0003-0097-5716

Ruquan Ye: ruquanye@cityu.edu.hk; ORCID: 0000-0002-2543-9090

Table of Contents

1. Supplementary Figure 1-64……..……..…3
2. Supplementary Table 1-6……..……..……..……..67
3. Supplementary Method……..……..……..…….73
4. Supplementary References……...……..……. ……...…74

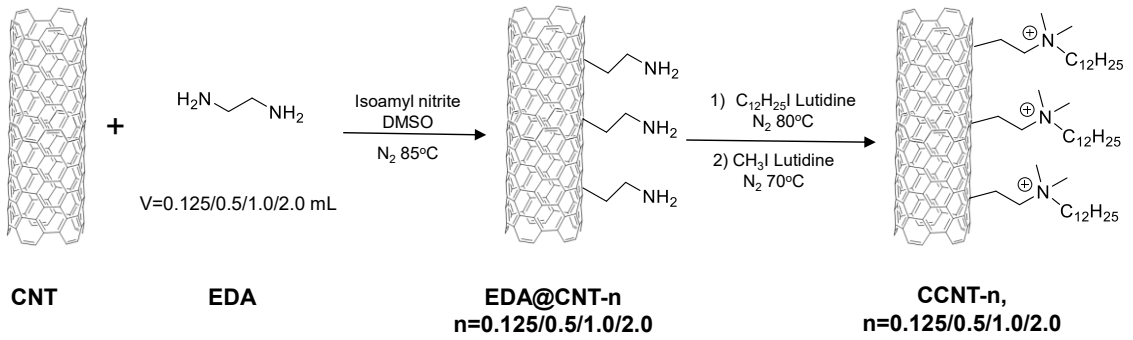

Supplementary Figure 1. Scheme for the synthesis of CCNT-n (n=0.125, 0.5, 1.0 and 2.0).

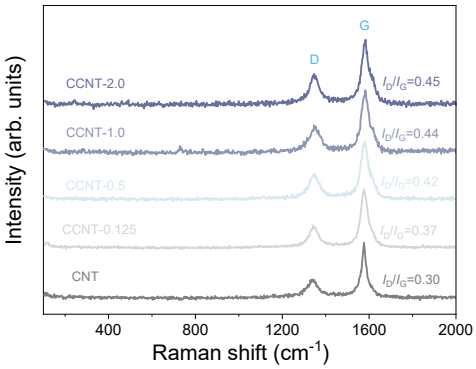

Supplementary Figure 2. Raman spectra of pristine CNT, CCNT-0.125, CCNT-0.5, CCNT-1.0 and CCNT-2.0. Source data are provided as a Source Data file.

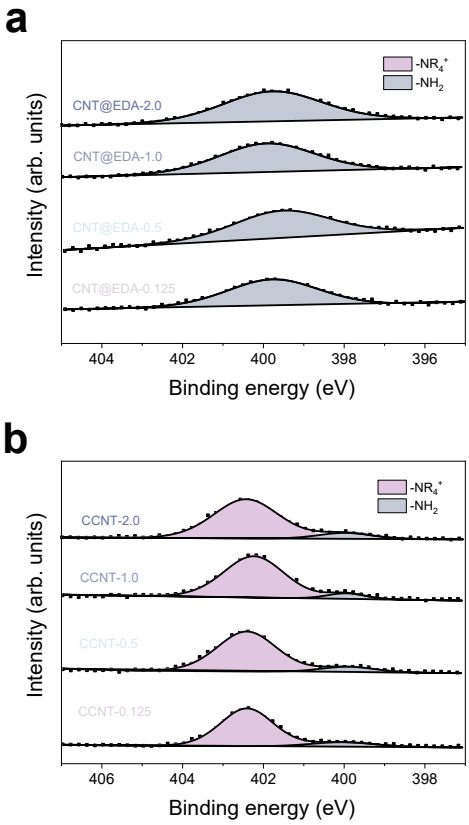

Supplementary Figure 3. N *1s* XPS spectra of (a) CNT@EDA-0.125, CNT@EDA-0.5, CNT@EDA-1.0 and CNT@EDA-2.0, (b) CCNT-0.125, CCNT-0.5, CCNT-1.0 and CCNT-2.0. Source data are provided as a Source Data file.

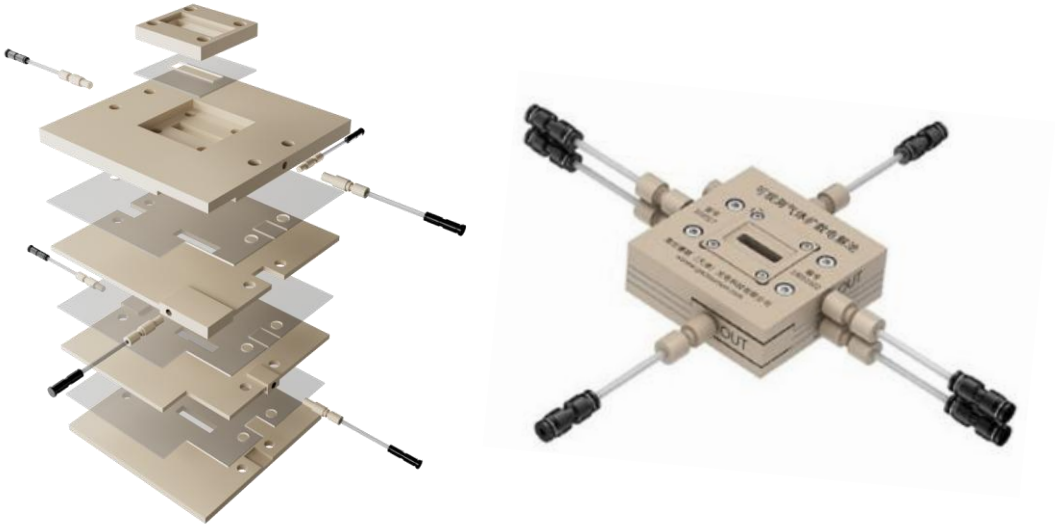

Supplementary Figure 4. Schematic representation of a three-compartment flow cell electrolyzer with indications of the transport directions for electrolytes.

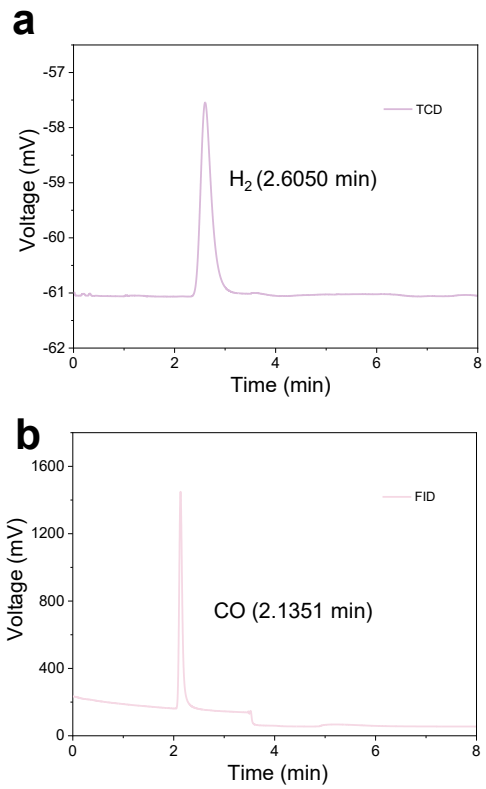

Supplementary Figure 5. Representative GC trace of the gaseous products formed on Bi/CCNT during acidic CO_2RR. (a) TCD, (b) FID signals of gaseous products. The retention times at 2.6050 min in TCD corresponded to the signal of H_2. CO was quantified by FID with retention times at 2.1351 min. Source data are provided as a Source Data file.

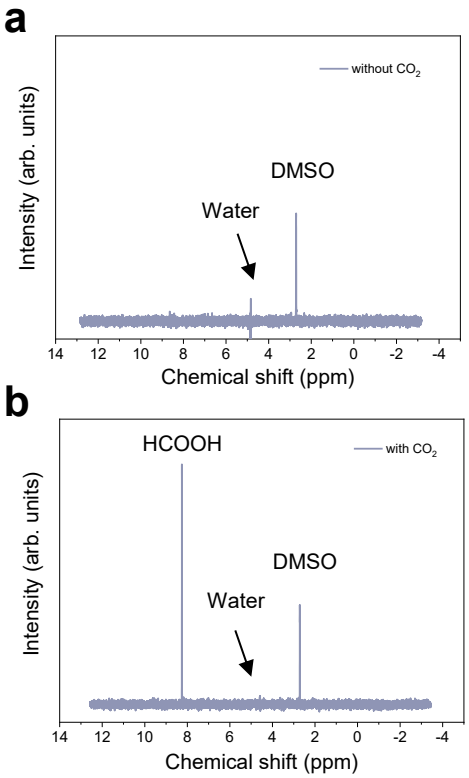

Supplementary Figure 6. ^{1}H NMR spectra of products using (a) no CO_2 and (b) CO_2 in 0.05 M H_2SO_4 + 3.0 M KCl over Bi/CCNT. The chemical shifts at 8.26, 4.85 and 2.71 ppm were attributed to the H in HCOOH, D_2O and DMSO, respectively. Source data are provided as a Source Data file.

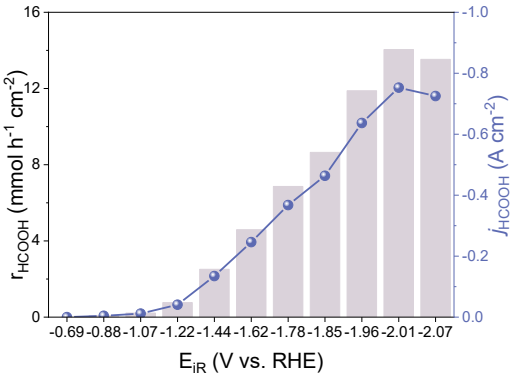

Supplementary Figure 7. Partial HCOOH current densities and HCOOH production rates for Bi/CCNT, catholyte: 0.05 M H_2SO_4 + 3.0 M KCl, anolyte: 0.1 M H_2SO_4, all reported potentials are manually iR-compensated at 85% (solution resistance: 2.2±0.1 Ω (n=3)). Source data are provided as a Source Data file.

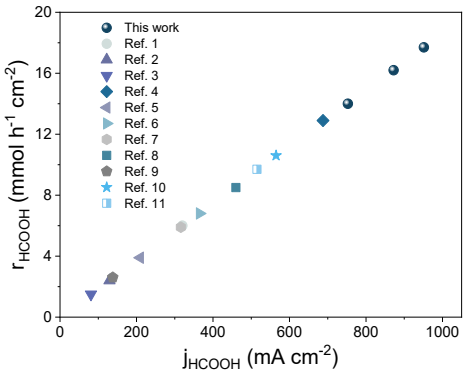

Supplementary Figure 8. Linear curve of reported j_{HCOOH} against r_{HCOOH}. Source data are provided as a Source Data file.

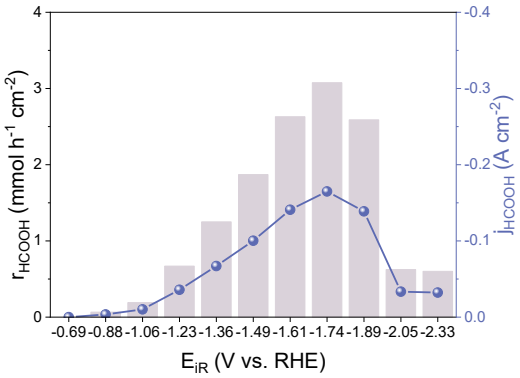

Supplementary Figure 9. Partial HCOOH current densities (j_{HCOOH}) and HCOOH production rates (r_{HCOOH}) for Bi/CNT, catholyte: 0.05 M H_2SO_4 + 3.0 M KCl, anolyte: 0.1 M H_2SO_4, all reported potentials are manually iR-compensated at 85% (solution resistance: 2.2±0.1 Ω (n=3)). Source data are provided as a Source Data file.

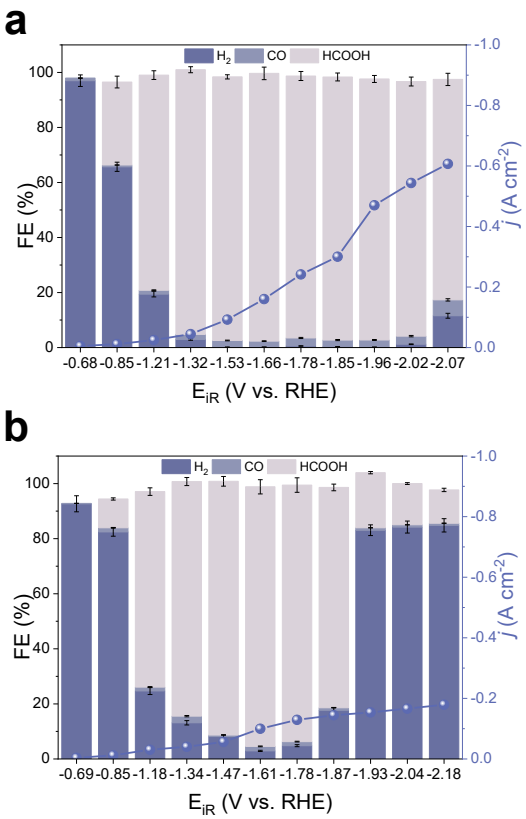

Supplementary Figure 10. Total current density curves and FE values of CO_2RR products for (a) Bi/CCNT and (b) Bi/CNT, catholyte: 0.05 M H_2SO_4 + 0.5 M KCl, anolyte: 0.1 M H_2SO_4, all reported potentials are manually iR-compensated at 85% (solution resistance: 4.7±0.2 Ω (n=3)). Source data are provided as a Source Data file.

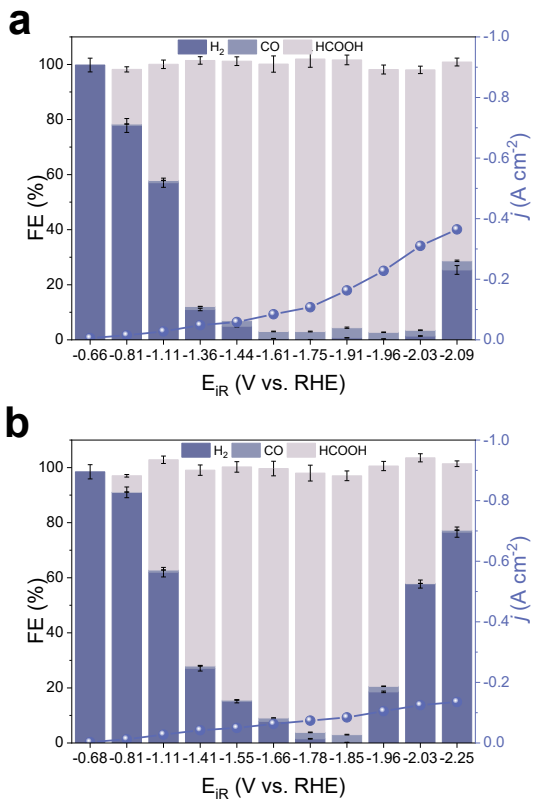

Supplementary Figure 11. Total current density curves and FE values of CO_2RR products for (a) Bi/CCNT and (b) Bi/CNT, catholyte: 0.05 M H_2SO_4 + 0.1 M KCl, anolyte: 0.1 M H_2SO_4, all reported potentials are manually iR-compensated at 85% (solution resistance: 8.2±0.2 Ω (n=3)). Source data are provided as a Source Data file.

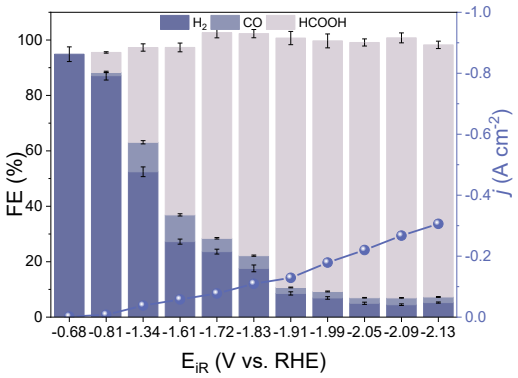

Supplementary Figure 12. Total current density curves and FE values of CO_2RR products for Bi/CCNT, catholyte: 0.05 M H_2SO_4 + 0.01 M KCl, anolyte: 0.1 M H_2SO_4, all reported potentials are manually iR-compensated at 85% (solution resistance: 14.1±0.3 Ω (n=3)). Source data are provided as a Source Data file.

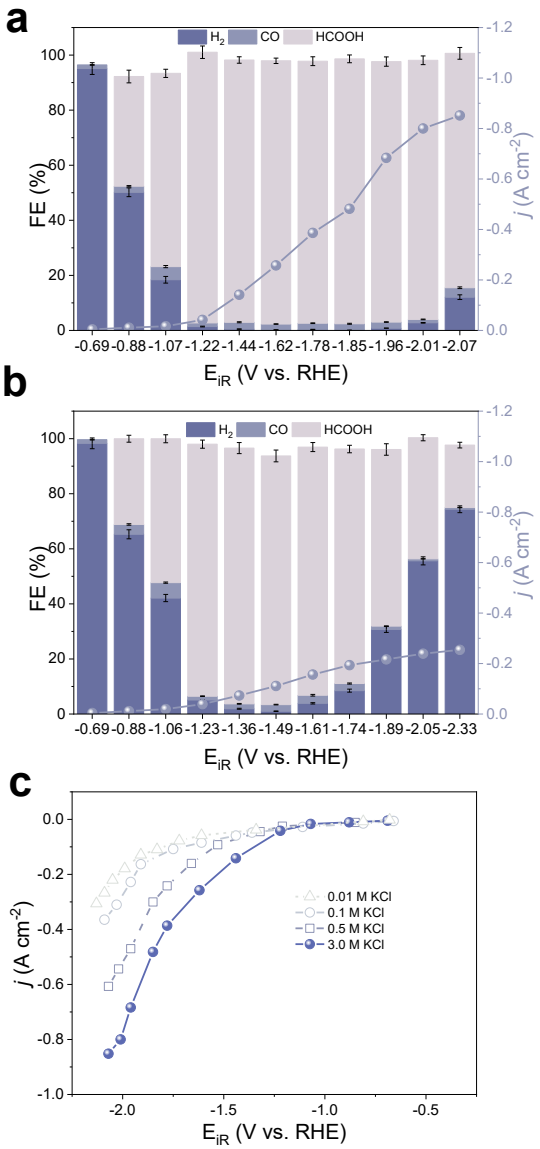

Supplementary Figure 13. Total current density curves and FE values of CO_2RR products in 0.05 M H_2SO_4 + 3.0 M KCl for (a) Bi/CCNT and (b) Bi/CNT, (c) Total current density curves of Bi/CCNT in 0.05 M H_2SO_4 with various K^+ concentrations, anolyte: 0.1 M H_2SO_4, all reported potentials are manually iR-compensated at 85%. Source data are provided as a Source Data file.

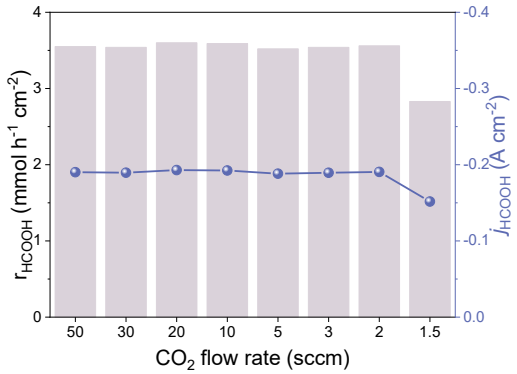

Supplementary Figure 14. Partial HCOOH current density and HCOOH production rate at different CO_2 gas flow rates under a total current density of -200 mA cm^{-2}, catholyte: 0.05 M H_2SO_4 + 3.0 M KCl, anolyte: 0.1 M H_2SO_4. Source data are provided as a Source Data file.

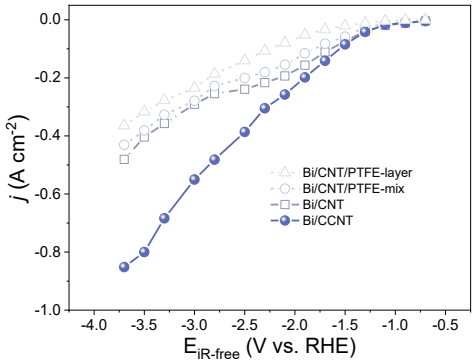

Supplementary Figure 15. Total current density curves of Bi/CNT/PTFE-layer, Bi/CNT/PTFE-mix, Bi/CNT and Bi/CCNT at different applied potentials, catholyte: 0.05 M H_2SO_4 + 3.0 M KCl, anolyte: 0.1 M H_2SO_4, the electrocatalytic performance was exhibited without iR compensation. Source data are provided as a Source Data file.

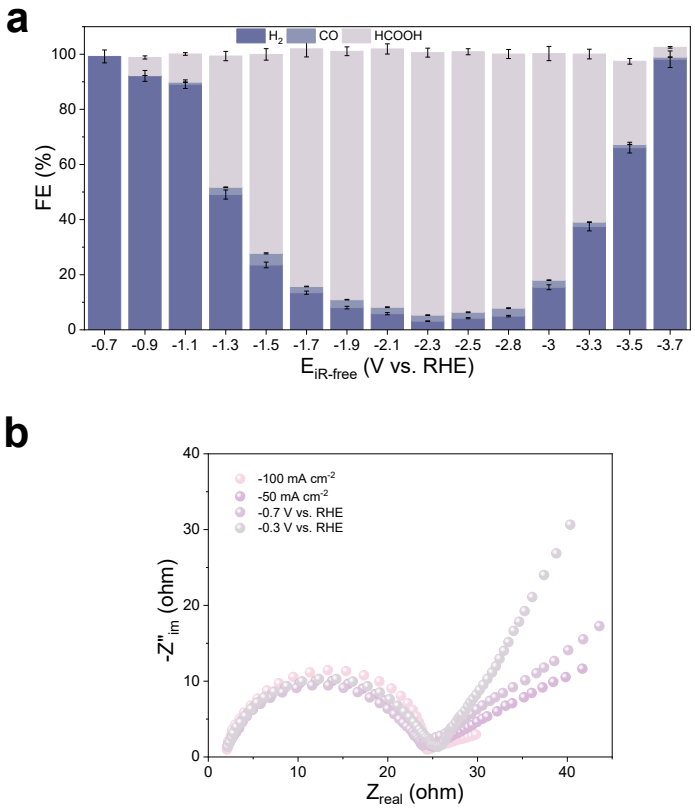

Supplementary Figure 16. (a) FE curves and (b) EIS measurements of Bi/CNT/PTFE-layer at different applied potentials, catholyte: 0.05 M H_2SO_4 + 3.0 M KCl, anolyte: 0.1 M H_2SO_4, the electrocatalytic performance was exhibited without iR compensation. Source data are provided as a Source Data file.

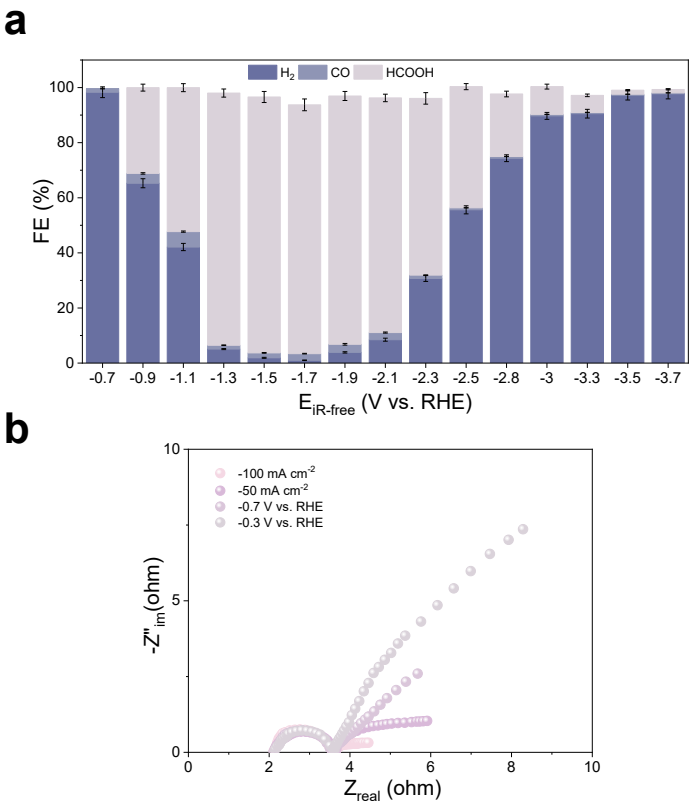

Supplementary Figure 17. (a) FE curves and (b) EIS measurements of Bi/CNT at different applied potentials, catholyte: 0.05 M H_2SO_4 + 3.0 M KCl, anolyte: 0.1 M H_2SO_4, the electrocatalytic performance was exhibited without iR compensation. Source data are provided as a Source Data file.

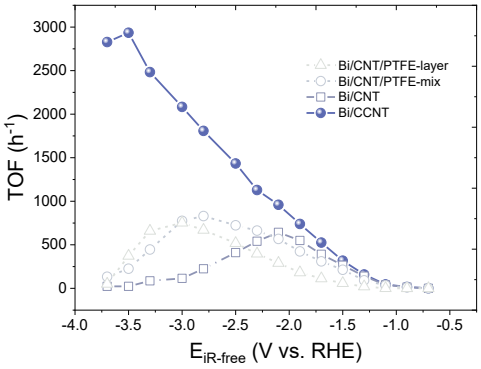

Supplementary Figure 18. TOF_{HCOOH} plots for Bi/CNT/PTFE-layer, Bi/CNT/PTFE-mix, Bi/CNT and Bi/CCNT, catholyte: 0.05 M H_2SO_4 + 3.0 M KCl, anolyte: 0.1 M H_2SO_4, the electrocatalytic performance was exhibited without iR compensation. Source data are provided as a Source Data file.

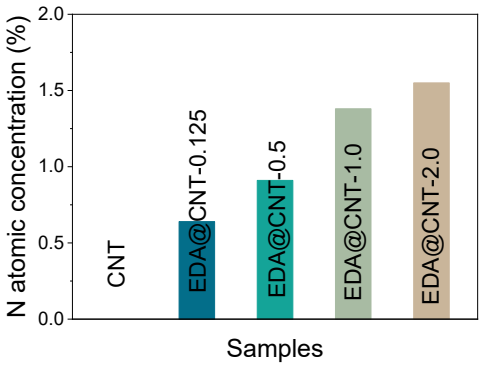

Supplementary Figure 19. The N atom concentration of various samples measured by XPS tests. Source data are provided as a Source Data file.

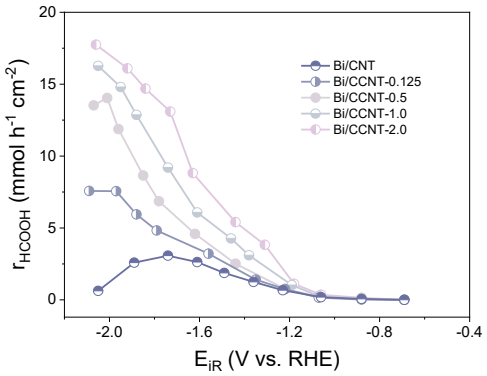

Supplementary Figure 20. HCOOH production rates for Bi/CNT, Bi/CCNT-0.125, Bi/CCNT-0.5, Bi/CCNT-1.0 and Bi/CCNT-2.0, catholyte: 0.05 M H_2SO_4 + 3.0 M KCl, anolyte: 0.1 M H_2SO_4, all reported potentials are manually iR-compensated at 85% (solution resistance: 2.2±0.1 Ω (n=3)). Source data are provided as a Source Data file.

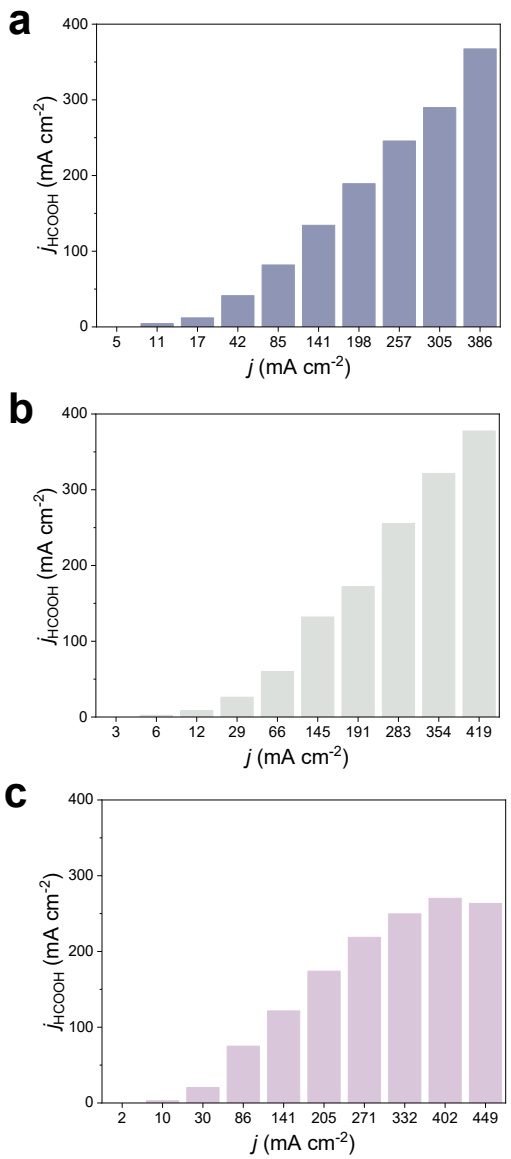

Supplementary Figure 21. The partial HCOOH current densities over Bi/CCNT in 0.05 M H_2SO_4 with (a) 3.0 M KCl, (b) 3.0 M $N(CH_3)_4Cl$ and (c) 3.0 M NH_4Cl, anolyte: 0.1 M H_2SO_4. Source data are provided as a Source Data file.

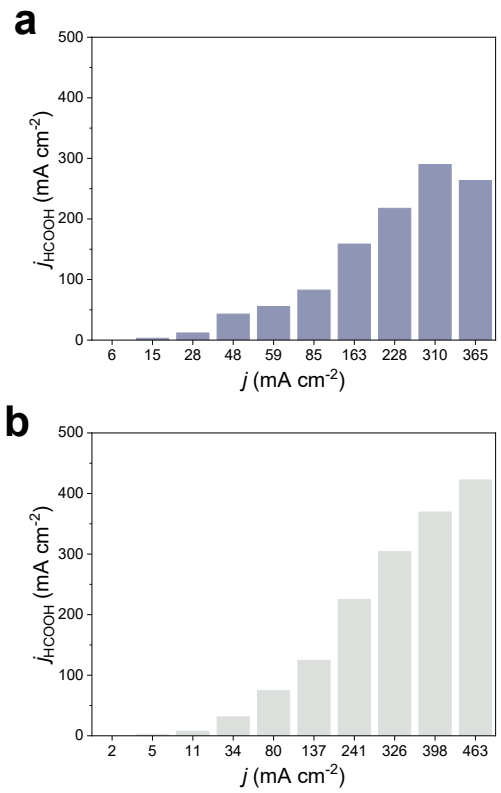

Supplementary Figure 22. The partial HCOOH current densities over Bi/CCNT in 0.05 M H_2SO_4 with (a) 0.1 M KCl and (b) 0.1 M KCl + 3.0 M $N(CH_3)_4Cl$, anolyte: 0.1 M H_2SO_4. Source data are provided as a Source Data file.

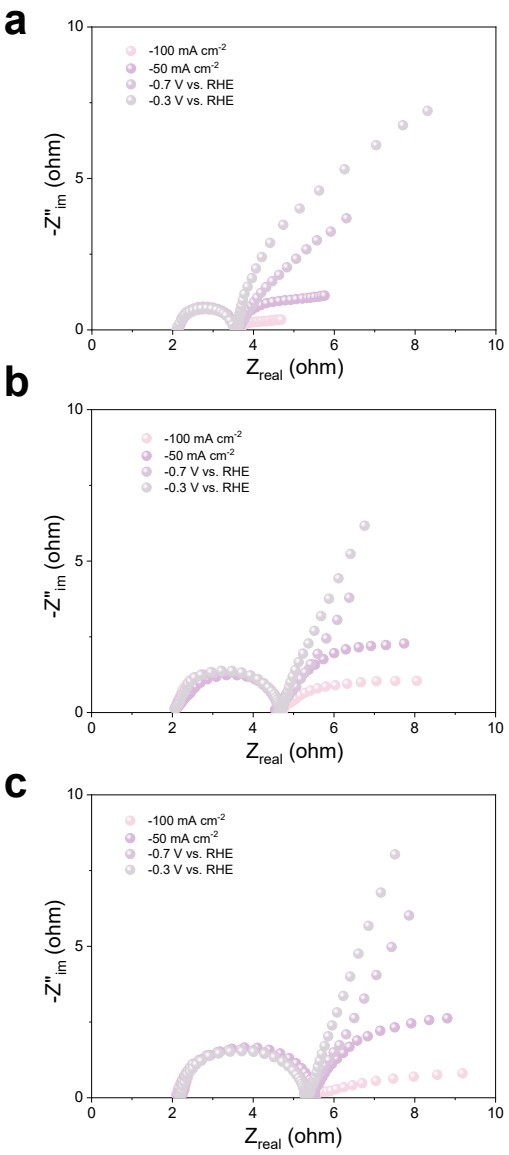

Supplementary Figure 23. Comparison of EIS measurements on Bi/CCNT in 0.05 M H_2SO_4 with different cations. (a) 3.0 M KCl, (b) 3.0 M $N(CH_3)_4Cl$ + 0.1 M KCl, (c) 3.0 M $N(CH_3)_4Cl$, anolyte: 0.1 M H_2SO_4. Source data are provided as a Source Data file.

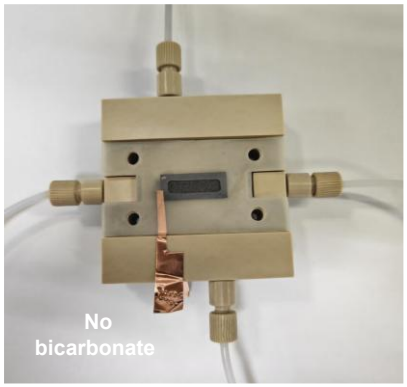

Supplementary Figure 24. Photo of the back side of gas diffusion electrode after 130-h stability test showing no salt deposition in the acidic electrolyte of $N(CH_3)_4^+$.

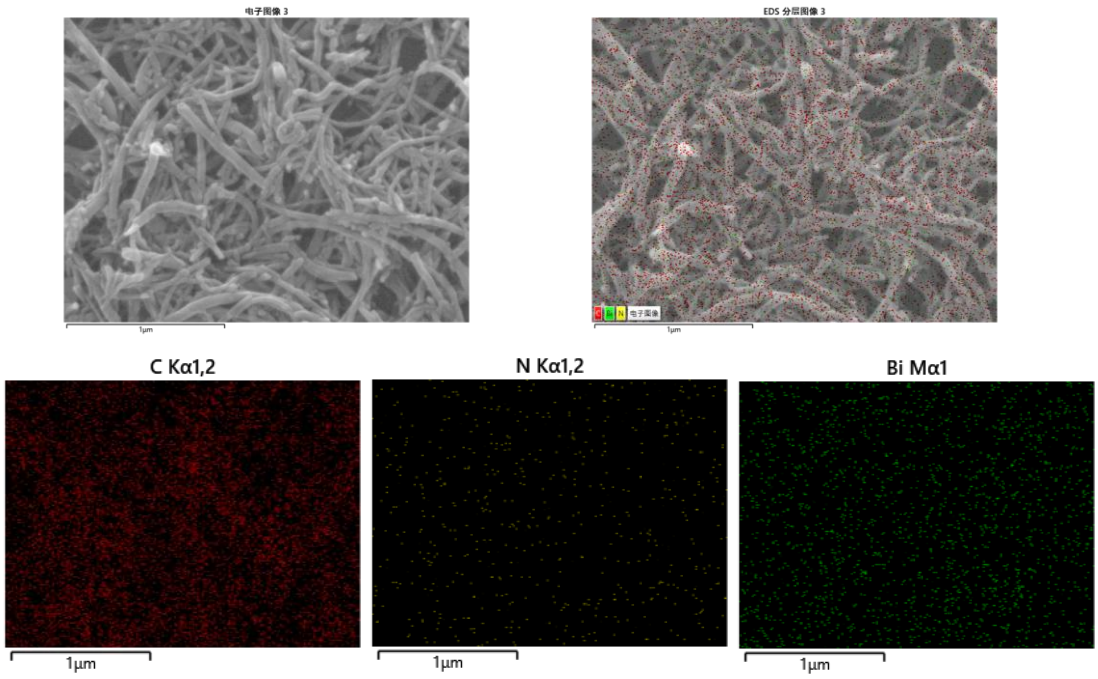

Supplementary Figure 25. SEM characterizations of the catalyst after 130 hours stability test. Scale bar: 500 nm.

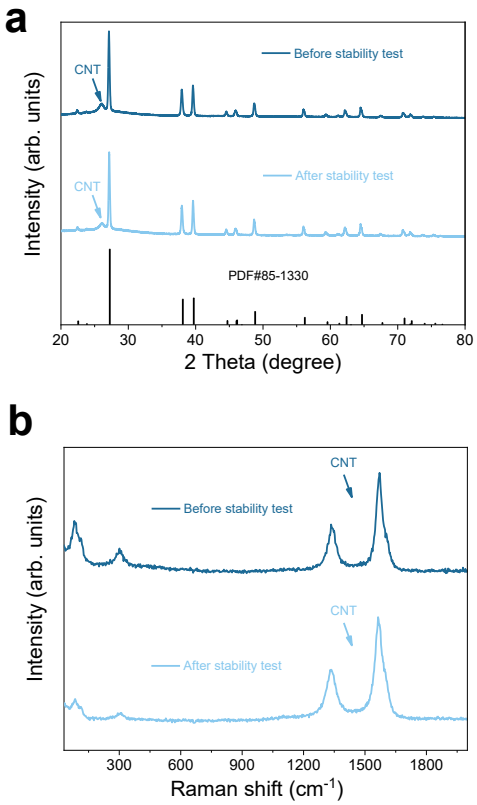

Supplementary Figure 26. (a) XRD spectra and (b) Raman spectra of Bi/CCNT before and after long-term stability test at around 280 mA cm^{-2}. Source data are provided as a Source Data file.

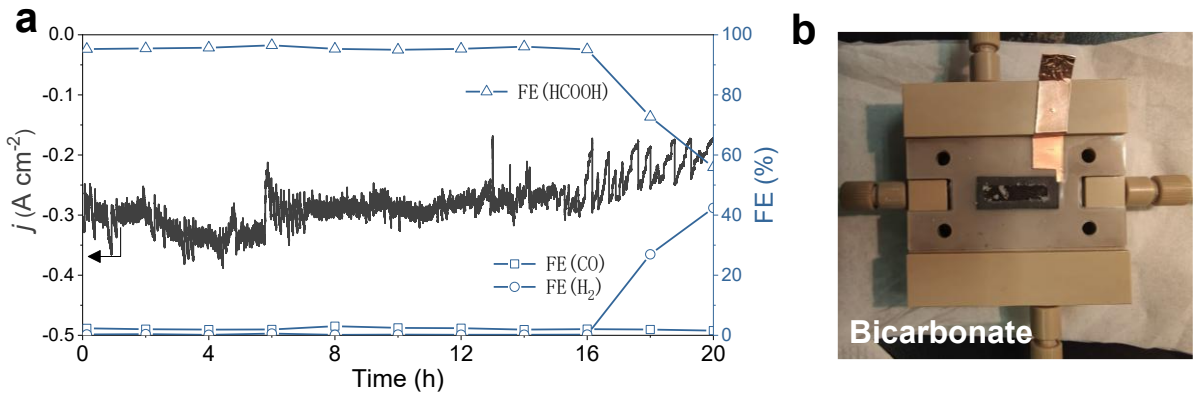

Supplementary Figure 27. (a) FE and current density for stability test using Bi/CCNT in 0.05 M H_2SO_4 + 3.0 M KCl, anolyte: 0.1 M H_2SO_4, (b) Photo of the back side of gas diffusion electrode after stability test showing salt deposition in the acidic electrolyte of 3.0 M K^+. Source data are provided as a Source Data file.

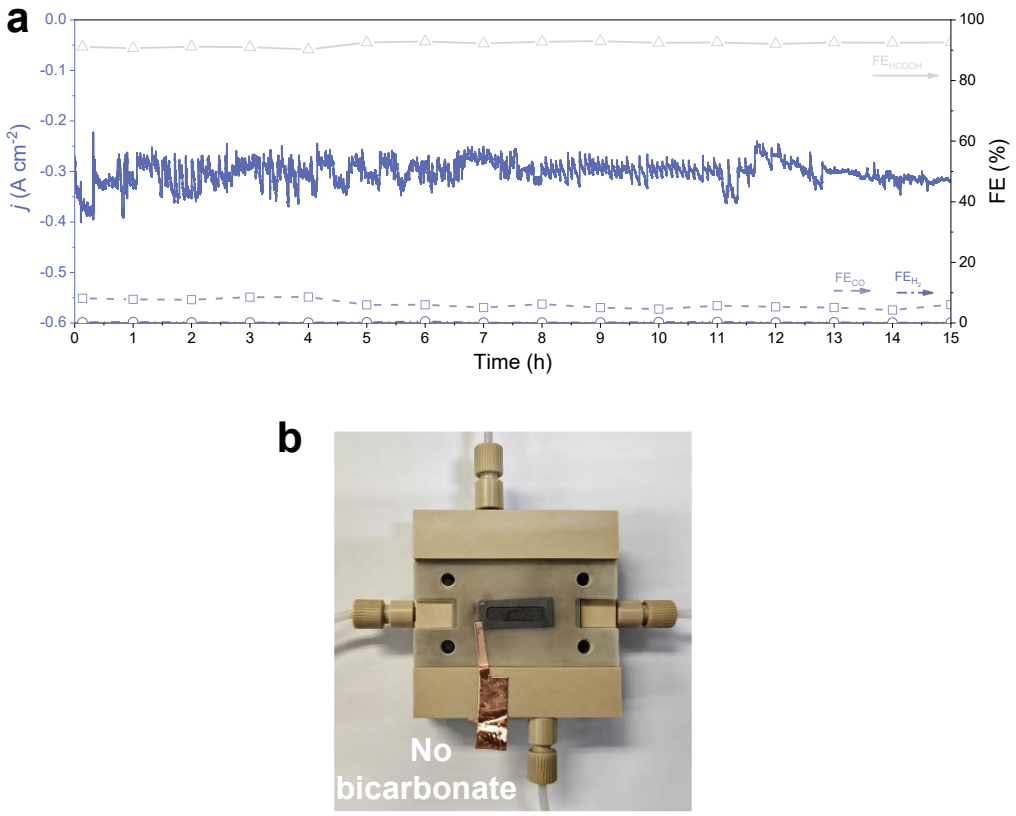

Supplementary Figure 28. (a) FE and current density for stability test using Bi/CCNT in 0.05 M H_2SO_4 + 0.1 M KCl + 3.0 M $N(CH_3)_4Cl$, anolyte: 0.1 M H_2SO_4, (b) Photo of the back side of gas diffusion electrode after stability test showing no salt deposition in the acidic electrolyte of 0.1 M K^+ + 3.0 M $N(CH_3)_4^+$. Source data are provided as a Source Data file.

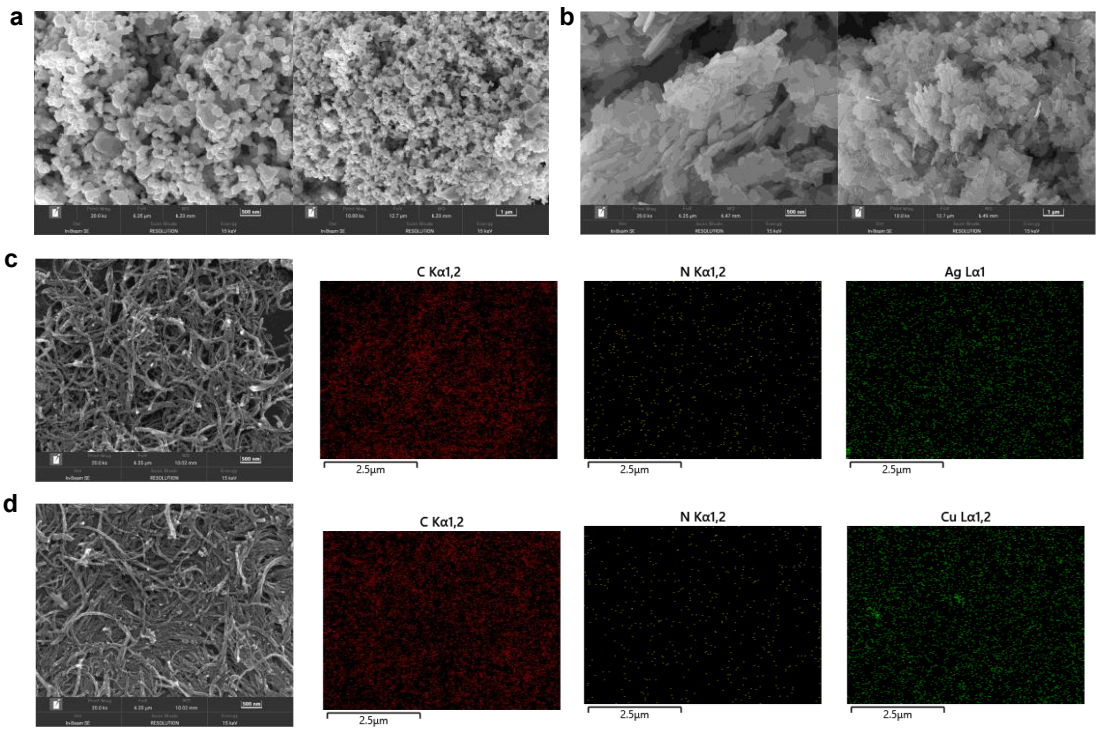

Supplementary Figure 29. SEM images of (a) Ag NS and (b) CuO NS. Scale bars: 500 nm and 1μm. EDS mapping of (c) Ag/CCNT and (d) CuO/CCNT. Scale bar: 500 nm.

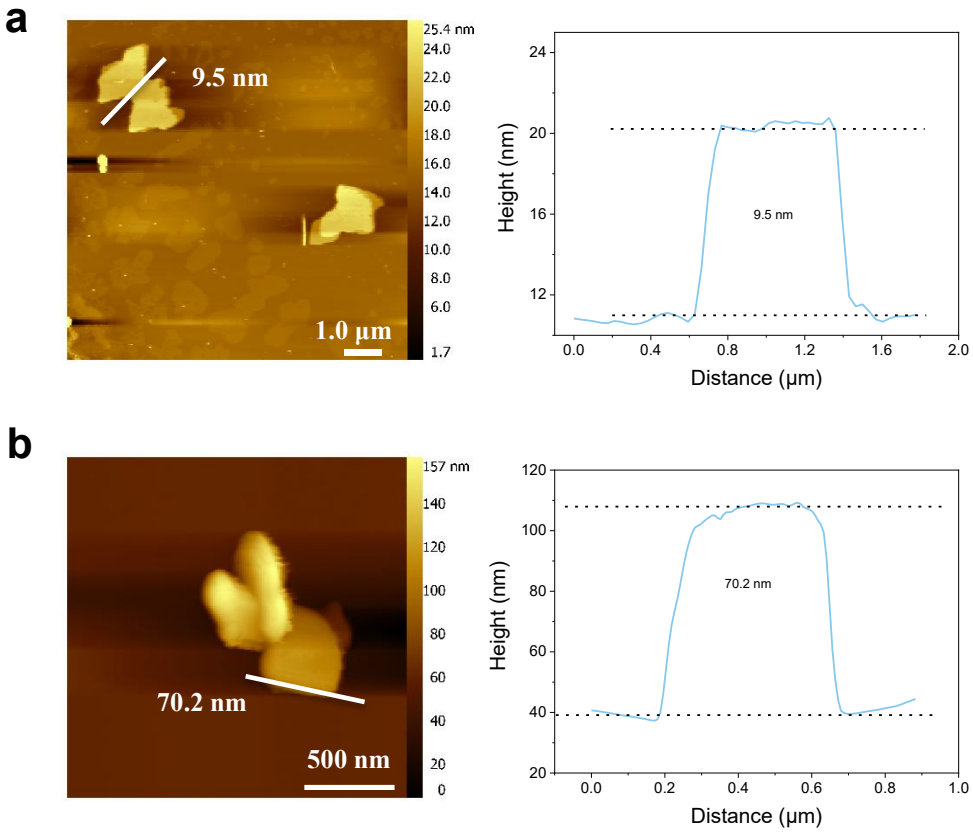

Supplementary Figure 30. AFM images of (a) Ag NS and (b) CuO NS. Source data are provided as a Source Data file.

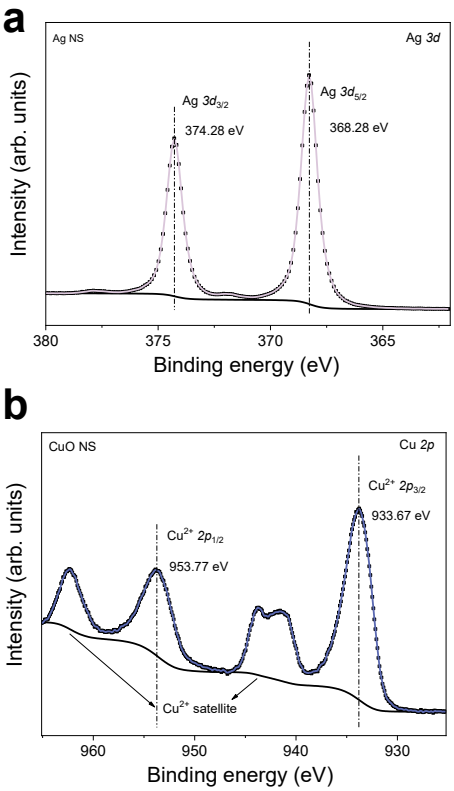

Supplementary Figure 31. XPS spectra of other metal catalysts for (a) Ag *3d* and (b) Cu *2p*. Source data are provided as a Source Data file.

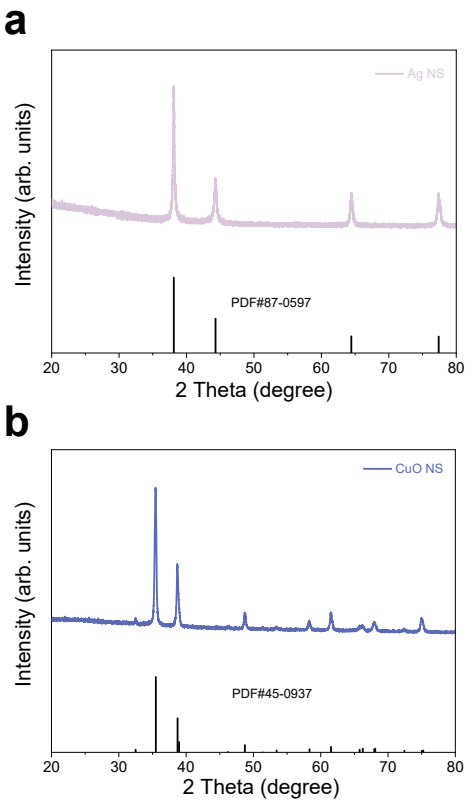

Supplementary Figure 32. XRD spectra of (a) Ag NS and (b) CuO NS. Source data are provided as a Source Data file.

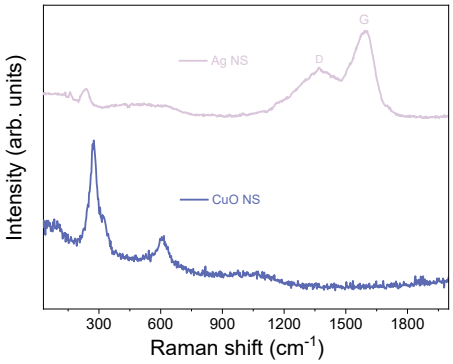

Supplementary Figure 33. Raman spectra of Ag NS and CuO NS. Source data are provided as a Source Data file.

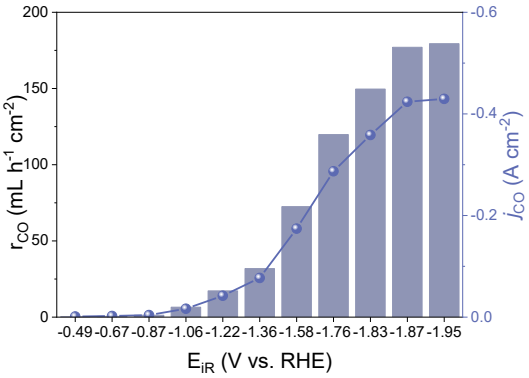

Supplementary Figure 34. Partial CO current densities and CO production rates for Ag/CCNT, catholyte: 0.05 M H_2SO_4 + 3.0 M KCl, anolyte: 0.1 M H_2SO_4, all reported potentials are manually iR-compensated at 85% (solution resistance: 2.2±0.1 Ω (n=3)). Source data are provided as a Source Data file.

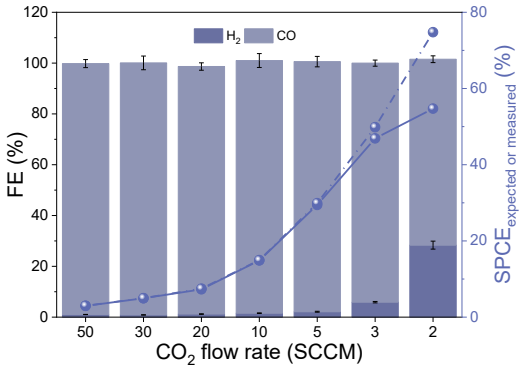

Supplementary Figure 35. SPCE and FE for Ag/CCNT at different CO_2 gas flow rates under a total current density of -200 mA cm^{-2}. Source data are provided as a Source Data file.

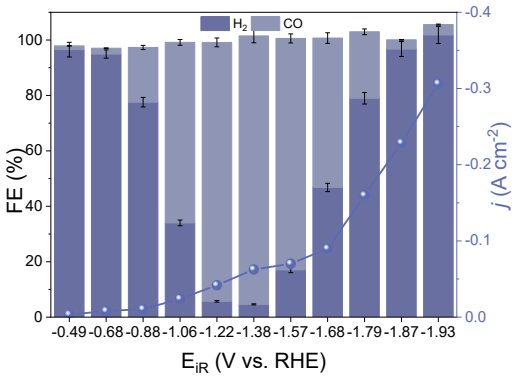

Supplementary Figure 36. Total current density curves and FE values of CO_2RR products for Ag/CNT, catholyte: 0.05 M H_2SO_4 + 3.0 M KCl, anolyte: 0.1 M H_2SO_4, all reported potentials are manually iR-compensated at 85% (solution resistance: 2.2±0.1 Ω (n=3)). Source data are provided as a Source Data file.

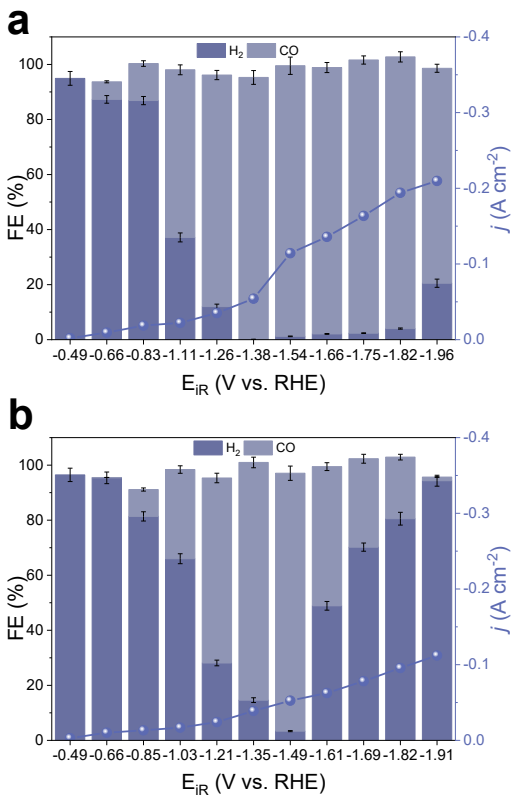

Supplementary Figure 37. Total current density curves and FE values of CO_2RR products for (a) Ag/CCNT and (b) Ag/CNT, catholyte: 0.05 M H_2SO_4 + 0.5 M KCl, anolyte: 0.1 M H_2SO_4, all reported potentials are manually iR-compensated at 85% (solution resistance: 4.7±0.2 Ω (n=3)). Source data are provided as a Source Data file.

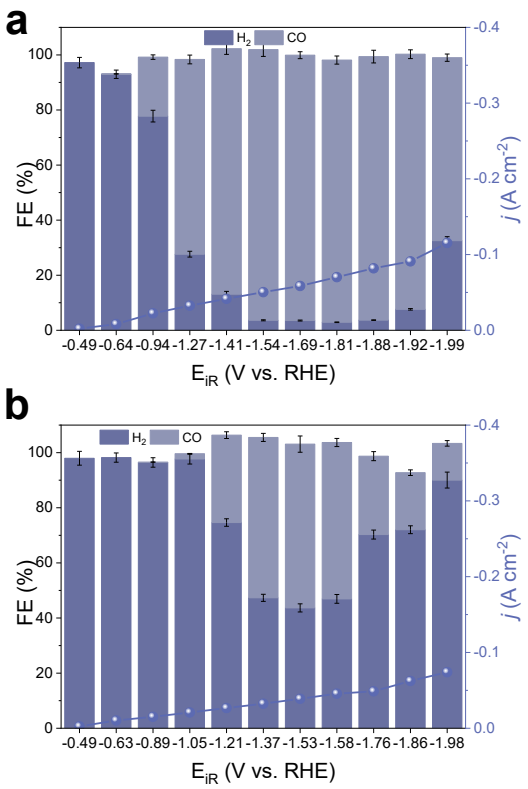

Supplementary Figure 38. Total current density curves and FE values of CO_2RR products for (a) Ag/CCNT and (b) Ag/CNT, catholyte: 0.05 M H_2SO_4 + 0.1 M KCl, anolyte: 0.1 M H_2SO_4, all reported potentials are manually iR-compensated at 85% (solution resistance: 8.2±0.2 Ω (n=3)). Source data are provided as a Source Data file.

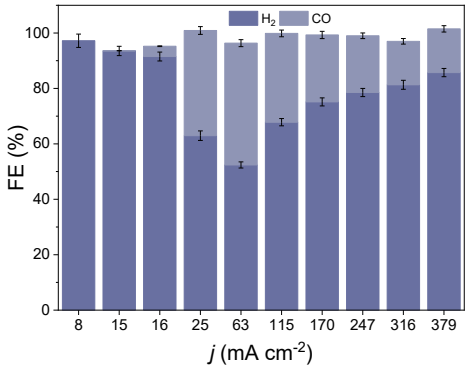

Supplementary Figure 39. FE values for Ag/CCNT in 0.05 M H_2SO_4 + 3.0 M NH_4Cl, anolyte: 0.1 M H_2SO_4. Source data are provided as a Source Data file.

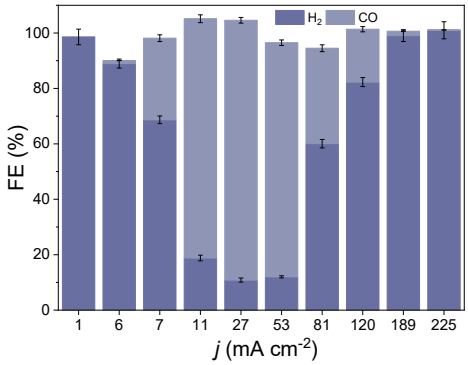

Supplementary Figure 40. FE values for Ag/CNT in 0.05 M H_2SO_4 + 3.0 M $N(CH_3)_4Cl$, anolyte: 0.1 M H_2SO_4. Source data are provided as a Source Data file.

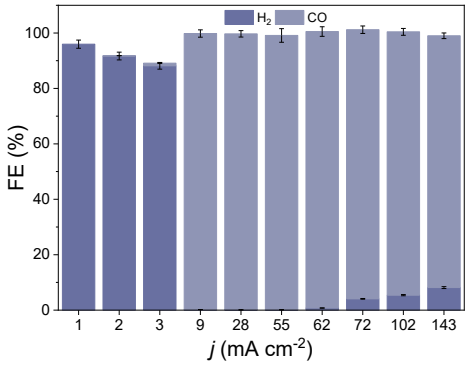

Supplementary Figure 41. FE values for Ag/CCNT in 0.05 M H_2SO_4 + 6.0 M $N(CH_3)_4Cl$, anolyte: 0.1 M H_2SO_4. Source data are provided as a Source Data file.

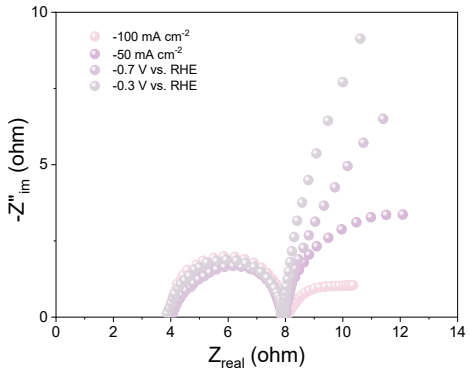

Supplementary Figure 42. EIS measurements on Ag/CCNT in 0.05 M H_2SO_4 + 6.0 M $N(CH_3)_4Cl$, anolyte: 0.1 M H_2SO_4. Source data are provided as a Source Data file.

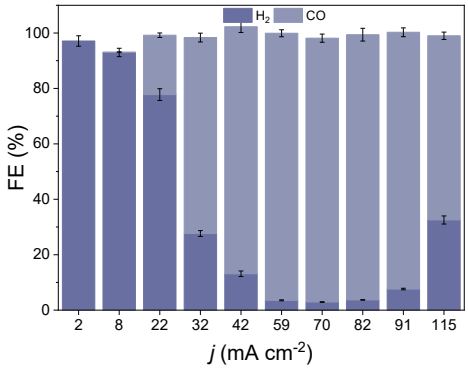

Supplementary Figure 43. FE values for Ag/CCNT in 0.05 M H_2SO_4 + 0.1 M KCl, anolyte: 0.1 M H_2SO_4.

Source data are provided as a Source Data file.

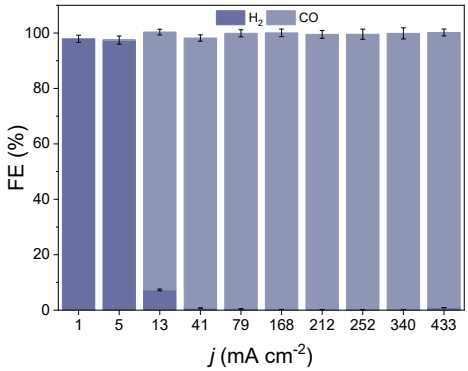

Supplementary Figure 44. FE values for Ag/CCNT in 0.05 M H_2SO_4 + 0.1 M KCl + 3.0 M $N(CH_3)_4Cl$, anolyte: 0.1 M H_2SO_4. Source data are provided as a Source Data file.

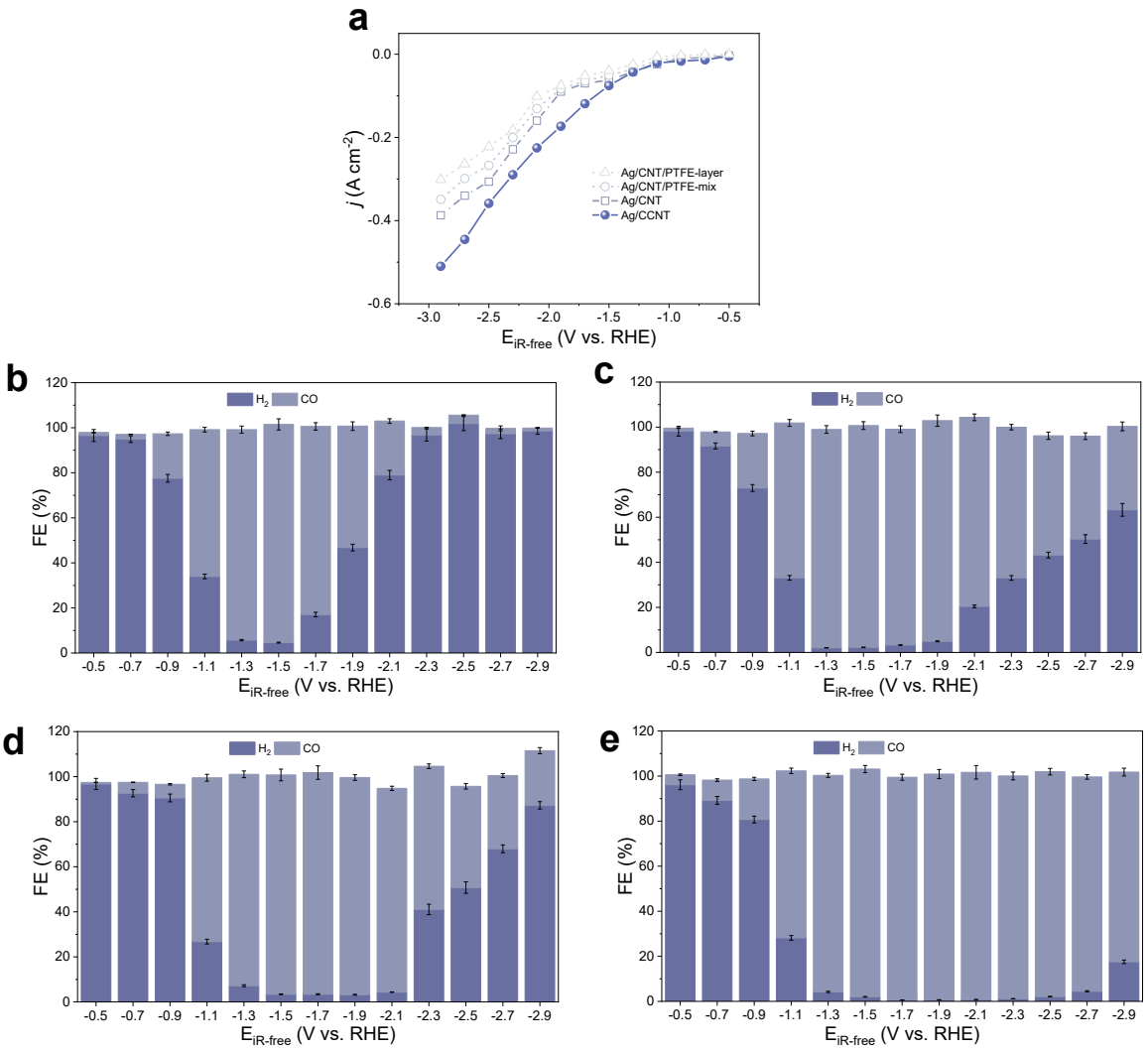

Supplementary Figure 45. (a) Total current density curves of Ag-derived catalysts at different applied potentials, (b-e) FE curves of (b) Ag/CNT, (c) Ag/CNT/PTFE-mix, (d) Ag/CNT/PTFE-layer and (e) Ag/CCNT at different applied potentials, catholyte: 0.05 M H_2SO_4 + 3.0 M KCl, anolyte: 0.1 M H_2SO_4, the electrocatalytic performance was exhibited without iR compensation. Source data are provided as a Source Data file.

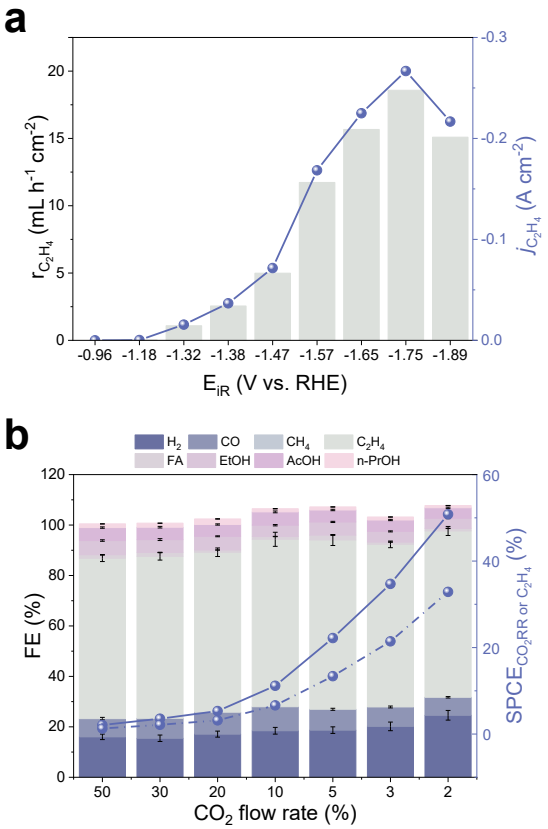

Supplementary Figure 46. (a) Partial C_2H_4 current densities and C_2H_4 production rates, catholyte: 0.05 M H_2SO_4 + 3.0 M KCl, anolyte: 0.1 M H_2SO_4, all reported potentials are manually iR-compensated at 85% (solution resistance: 2.2±0.1 Ω (n=3)), (b) SPCE and FE under a total current density of -400 mA cm^{-2} for CuO/CCNT in 0.05 M H_2SO_4 + 3.0 M KCl, anolyte: 0.1 M H_2SO_4. Source data are provided as a Source Data file.

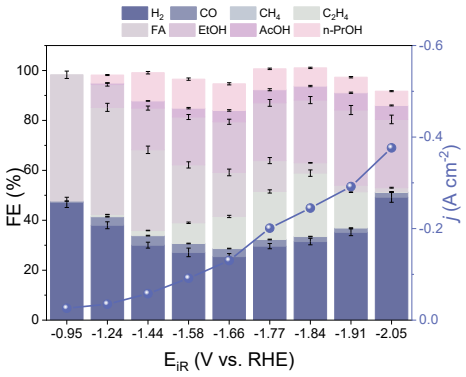

Supplementary Figure 47. Total current density curves and FE values of CO_2RR products for CuO/CNT, catholyte: 0.05 M H_2SO_4 + 3.0 M KCl, anolyte: 0.1 M H_2SO_4, all reported potentials are manually iR-compensated at 85% (solution resistance: 2.2±0.1 Ω (n=3)). Source data are provided as a Source Data file.

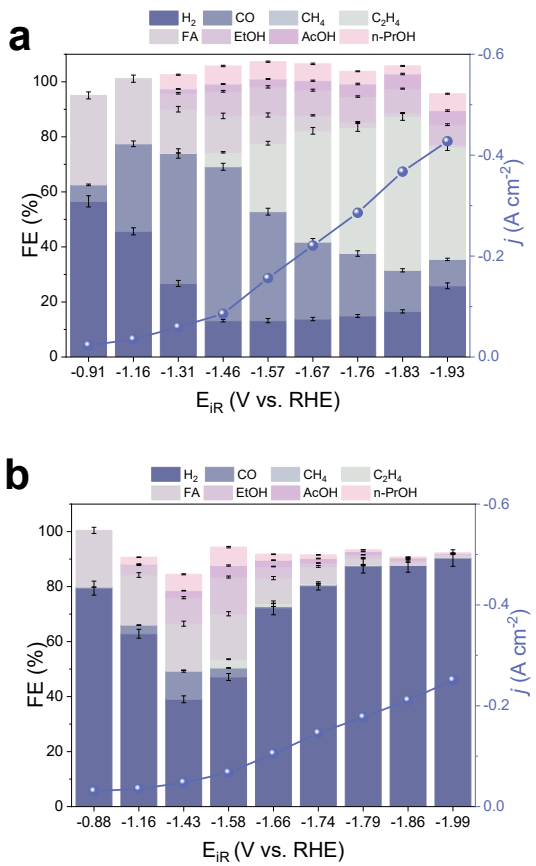

Supplementary Figure 48. Total current density curves and FE values of CO_2RR products for (a) CuO/CCNT and (b) CuO/CNT, catholyte: 0.05 M H_2SO_4 + 0.5 M KCl, anolyte: 0.1 M H_2SO_4, all reported potentials are manually iR-compensated at 85% (solution resistance: 4.7±0.2 Ω (n=3)). Source data are provided as a Source Data file.

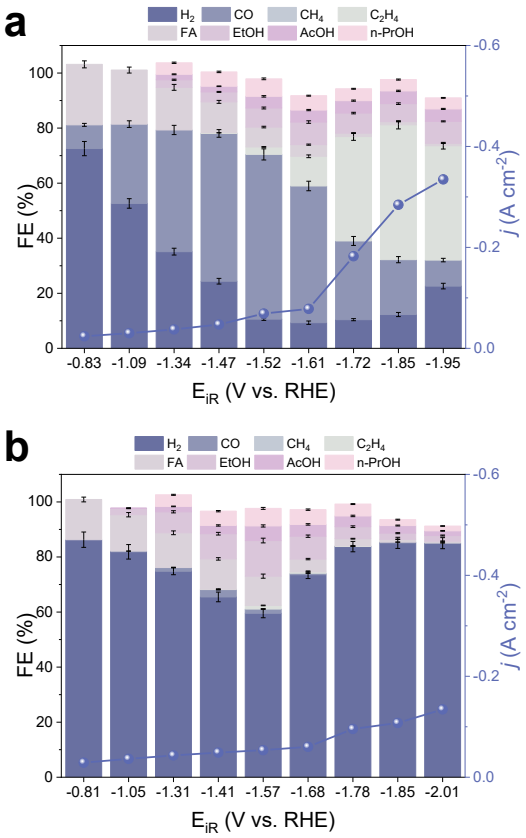

Supplementary Figure 49. Total current density curves and FE values of CO_2RR products for (a) CuO/CCNT and (b) CuO/CNT, catholyte: 0.05 M H_2SO_4 + 0.1 M KCl, anolyte: 0.1 M H_2SO_4, all reported potentials are manually iR-compensated at 85% (solution resistance: 8.2±0.2 Ω (n=3)). Source data are provided as a Source Data file.

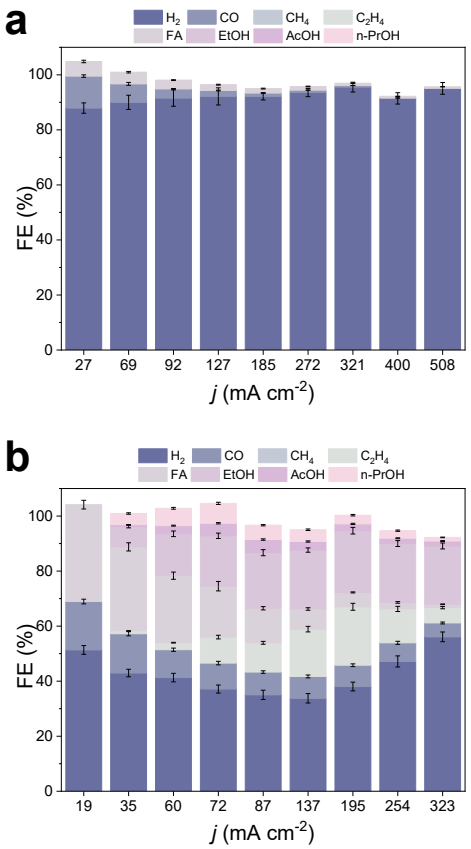

Supplementary Figure 50. FE values at different total current densities for (a) CuO/CCNT in 0.05 M H_2SO_4 + 3.0 M NH_4Cl, (b) CuO/CNT in 0.05 M H_2SO_4 + 3.0 M $N(CH_3)_4Cl$, anolyte: 0.1 M H_2SO_4. Source data are provided as a Source Data file.

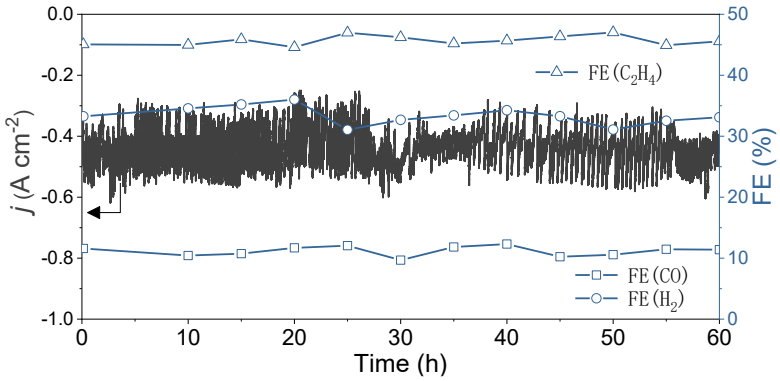

Supplementary Figure 51. FE and total current density for stability test using CuO/CCNT, catholyte: 0.05 M H_2SO_4 + 3.0 M $N(CH_3)_4Cl$, anolyte: 0.1 M H_2SO_4. Source data are provided as a Source Data file.

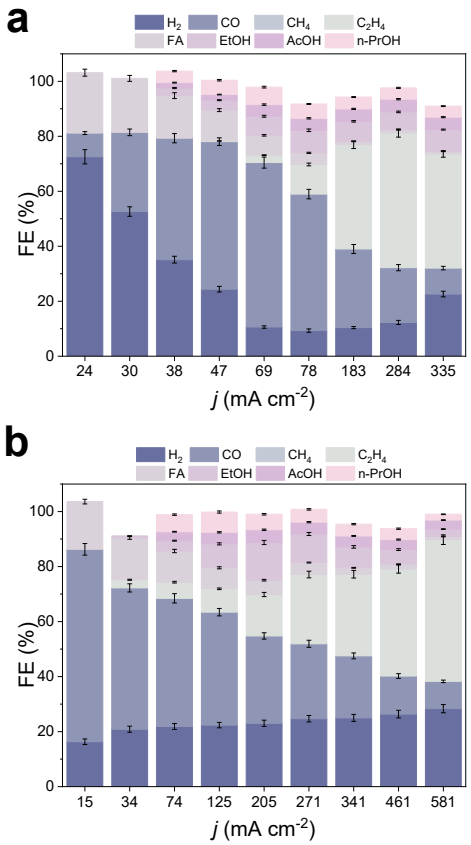

Supplementary Figure 52. FE values at different total current densities for CuO/CCNT in 0.05 M H_2SO_4 with (a) 0.1 M KCl and (b) 0.1 M KCl + 3.0 M $N(CH_3)_4Cl$, anolyte: 0.1 M H_2SO_4. Source data are provided as a Source Data file.

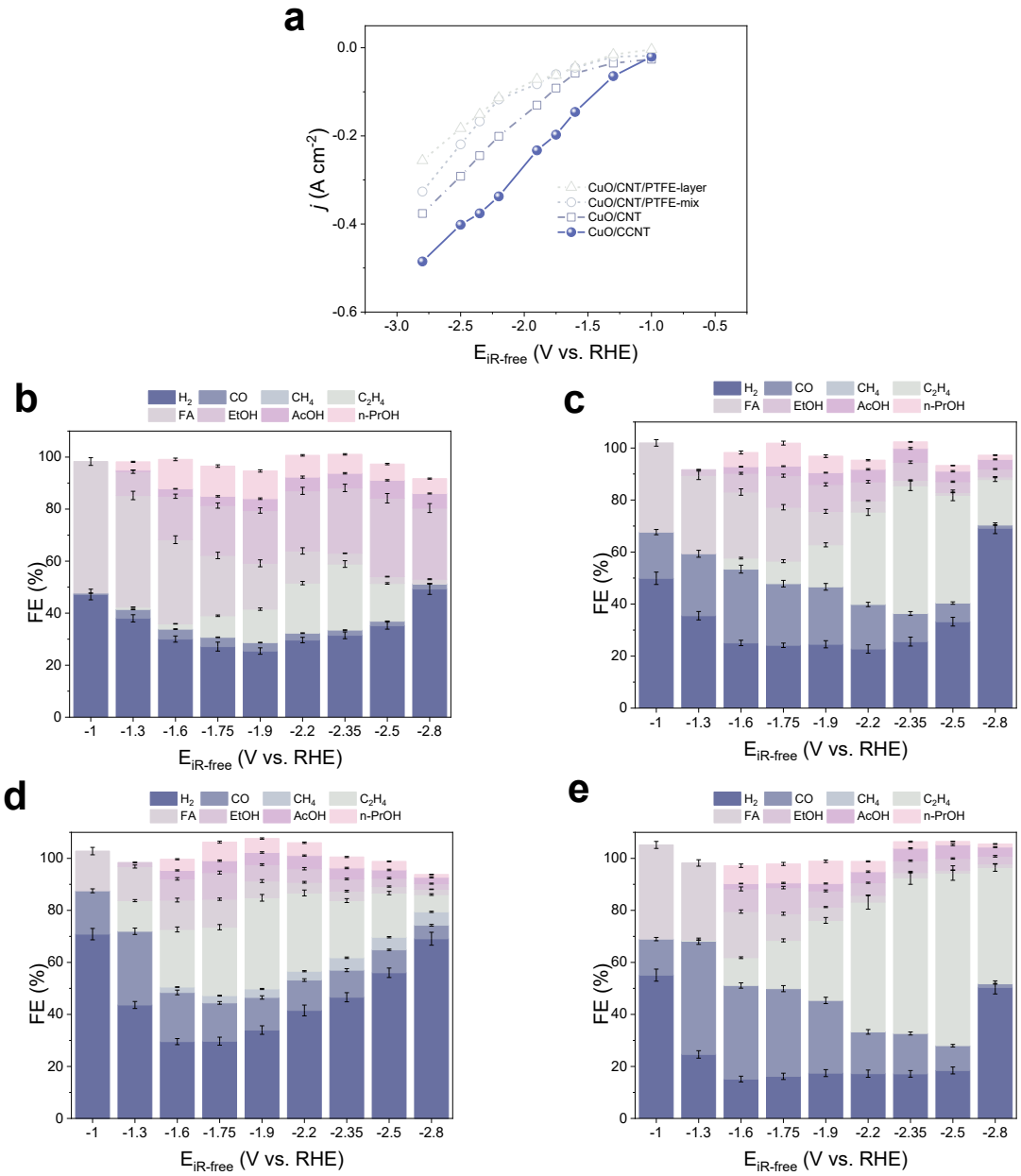

Supplementary Figure 53. (a) Total current density curves of CuO-derived catalysts at different applied potentials, (b-e) FE curves of (b) CuO/CNT, (c) CuO/CNT/PTFE-mix, (d) CuO/CNT/PTFE-layer and (e) CuO/CCNT at different applied potentials, catholyte: 0.05 M H_2SO_4 + 3.0 M KCl, anolyte: 0.1 M H_2SO_4, the electrocatalytic performance was exhibited without iR compensation. Source data are provided as a Source Data file.

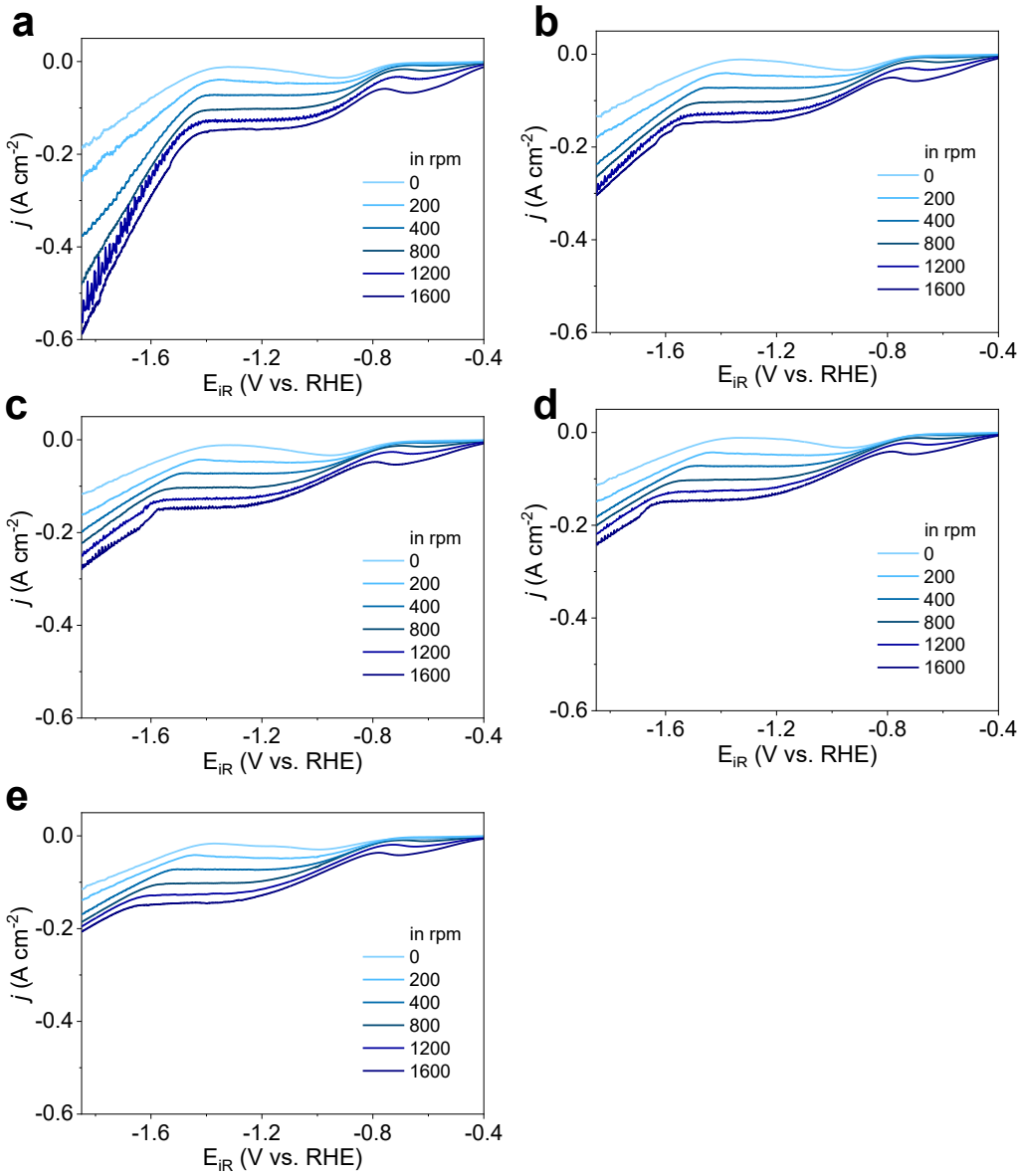

Supplementary Figure 54. HER LSV curves at varying rotating speed for (a) CNT, (b) CCNT-0.125, (c) CCNT-0.5, (d) CCNT-1.0 and (e) CCNT-2.0, electrolyte: 0.05 M H_2SO_4 + 0.5 M K_2SO_4, scan rate: 10 mV s^{-1}, all reported potentials are automatically iR-compensated at 85%. Source data are provided as a Source Data file.

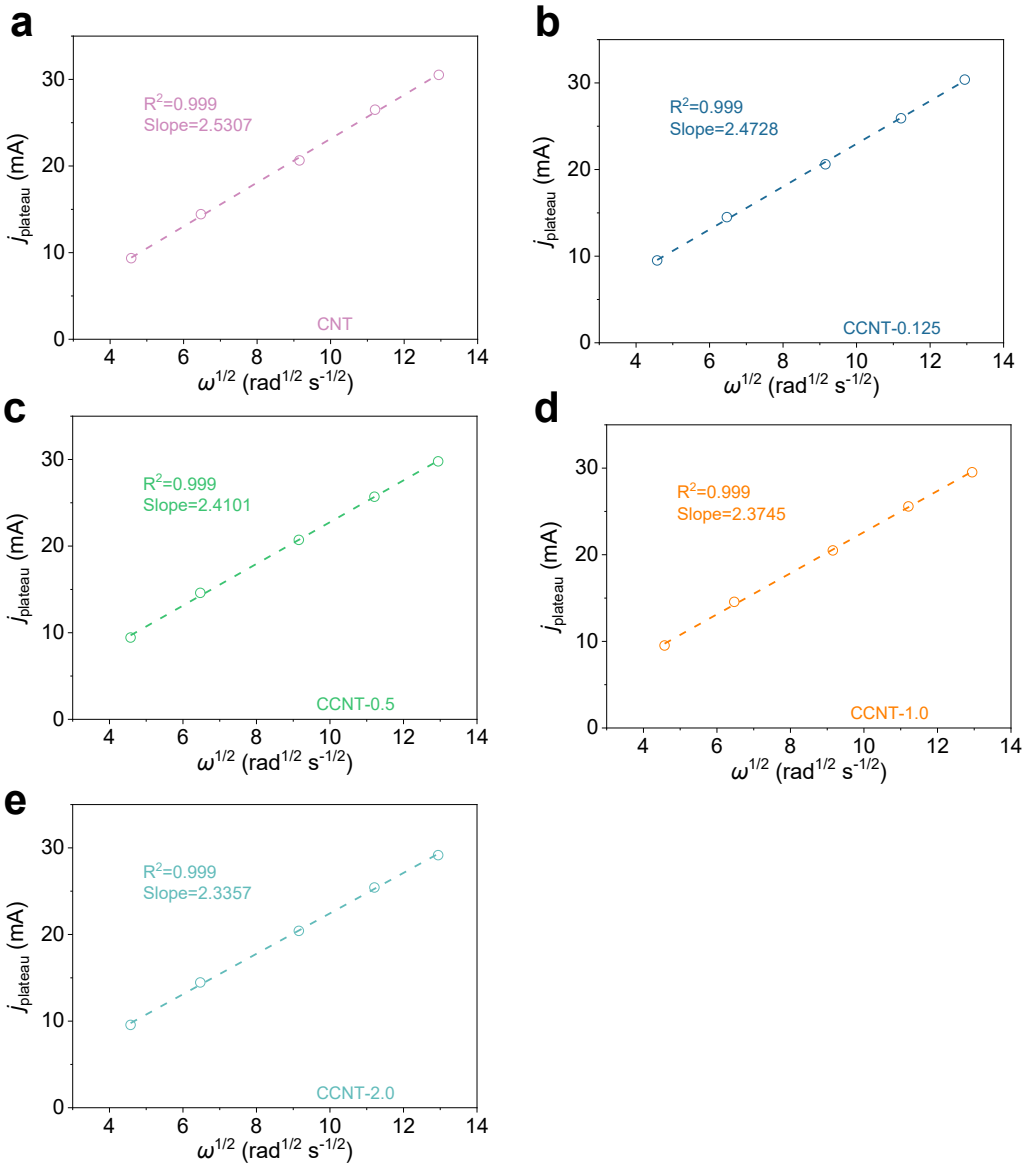

Supplementary Figure 55. Linear fitting of $j_{plateau}$ vs. $\omega^{1/2}$ for (a) CNT, (b) CCNT-0.125, (c) CCNT-0.5, (d) CCNT-1.0 and (e) CCNT-2.0 based on Levich equation. Source data are provided as a Source Data file.

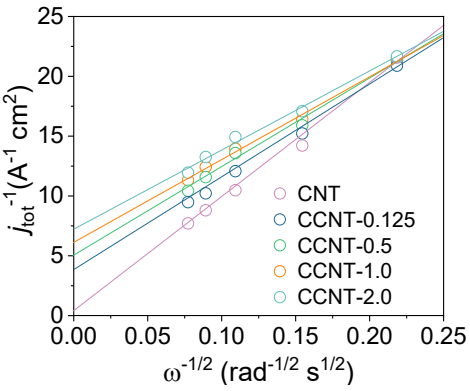

Supplementary Figure 56. Koutecký-Levich plot of different samples at -1.0 V_{iR}. Source data are provided as a Source Data file.

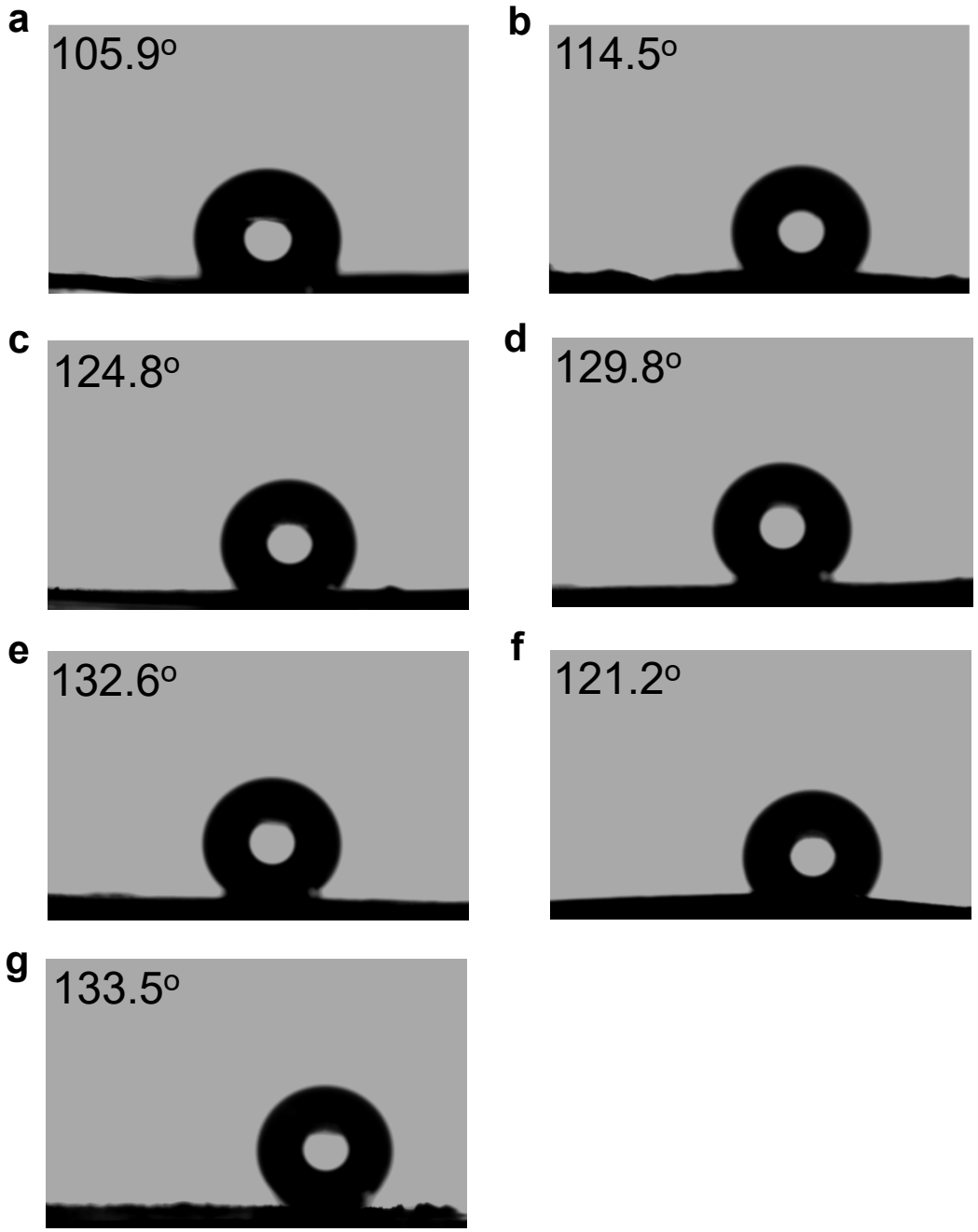

Supplementary Figure 57. Water contact angle measurements for (a) CNT, (b) CCNT-0.125, (c) CCNT-0.5, (d) CCNT-1.0, (e) CCNT-2.0, (f) CNT/PTFE-mix and (g) CNT/PTFE-layer.

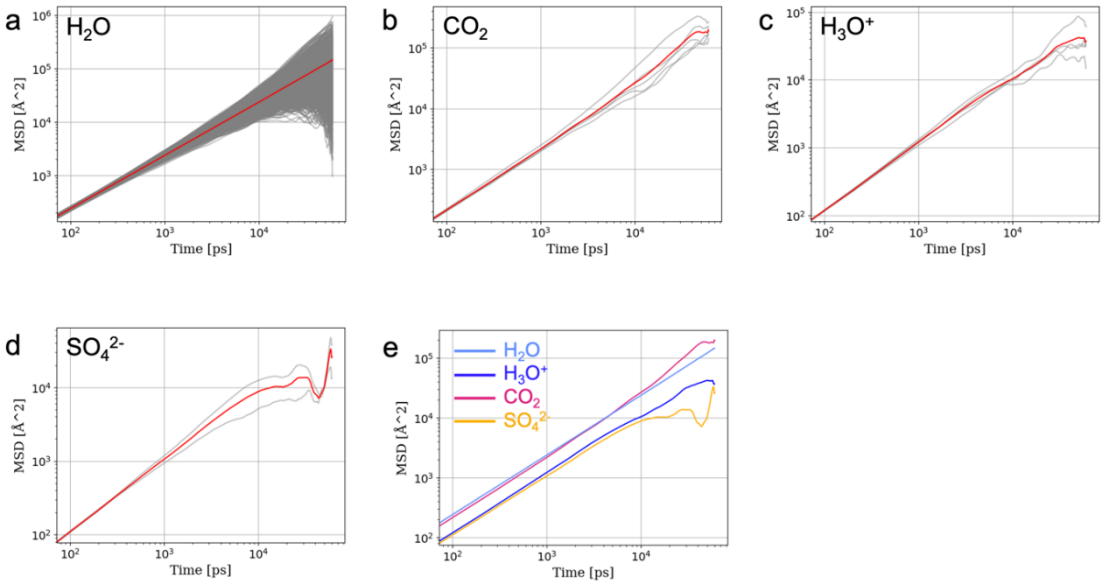

Supplementary Figure 58. Mean squared displacement for (a) H_2O, (b) CO_2, (c) H_3O^+, (d) SO_4^{2-}, and (e) all species without (C)CNT and Cl^- ion. Source data are provided as a Source Data file.

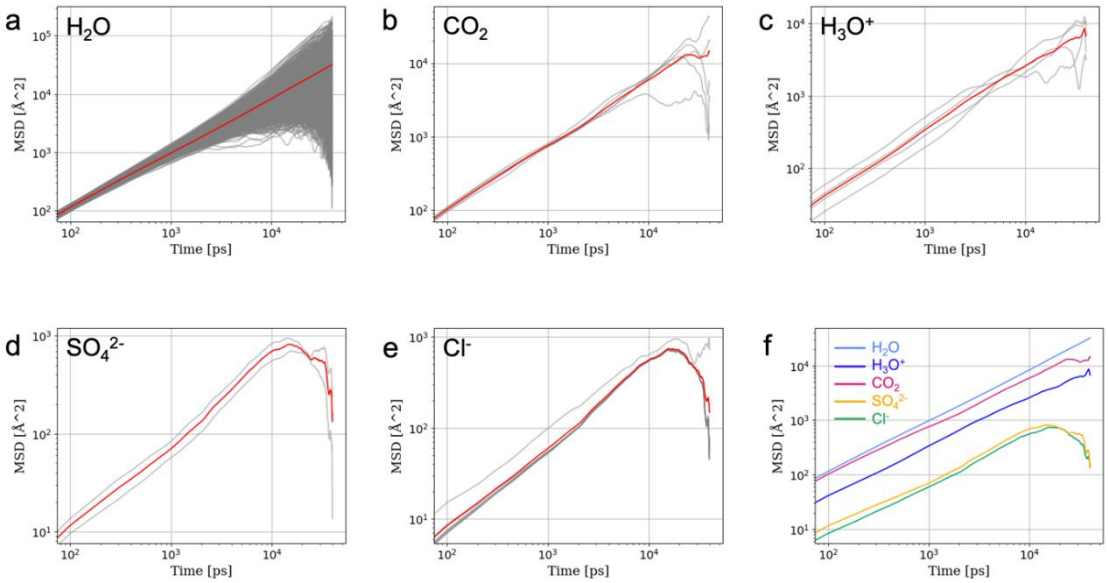

Supplementary Figure 59. Mean squared displacement for (a) H_2O, (b) CO_2, (c) H_3O^+, (d) SO_4^{2-}, (e) Cl^-, and (f) all species with (C)CNT. Source data are provided as a Source Data file.

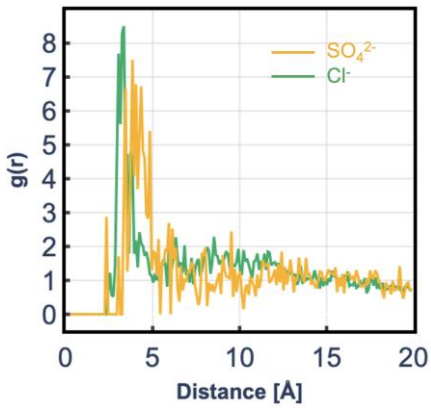

Supplementary Figure 60. Radial distribution function between hydronium ion (H_3O^+) and anions: SO_4^{2-} (yellow) and Cl^- (green). Source data are provided as a Source Data file.

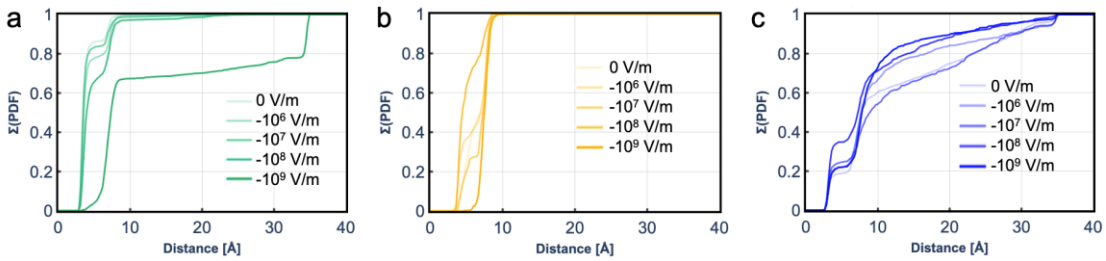

Supplementary Figure 61. Integration of probability density function with different electric field. (a) Cl^-, (b) SO_4^{2-}, and (c) H_3O^+. Source data are provided as a Source Data file.

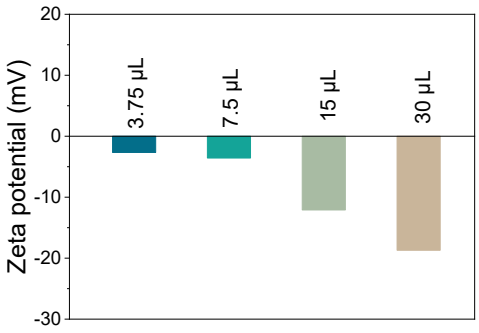

Supplementary Figure 62. Zeta potential of Nafion aqueous solutions with various amounts. Source data are provided as a Source Data file.

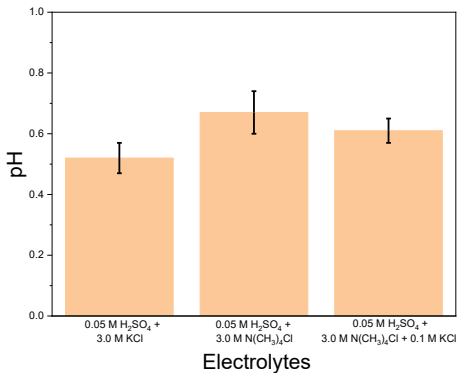

Supplementary Figure 63. Measured pH values for the three electrolyte solutions: 0.05 M H_2SO_4 + 3.0 M KCl, 0.05 M H_2SO_4 + 3.0 M $N(CH_3)_4Cl$ and 0.05 M H_2SO_4 + 3.0 M $N(CH_3)_4Cl$ + 0.1 M KCl. Source data are provided as a Source Data file.

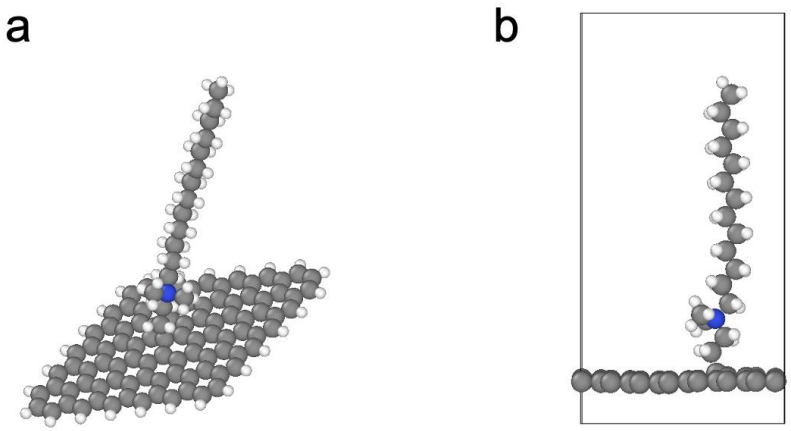

Supplementary Figure 64. (a) A finite cluster model and (b) a periodic model for molecular cation on graphene.

Supplementary Table 1. Performance metrics of various electrocatalysts for CO_2-to-HCOOH conversion in flow cell.

Catalyst	Electrolyte	pH	FE_{HCOOH} (%)	j_{HCOOH} (mA cm^{-2})	r_{HCOOH} (mmol h^{-1} cm^{-2})	Reference
Bi/CCNT	0.05 M H_2SO_4 + 3.0 M KCl	0.52	94.1	752.7	14.0	This work
Bi/CCNT-1.0			92.6	872.2	16.2	
Bi/CCNT-2.0			93.5	951.3	17.7	
In_2O_{3-x}@C	1.0 M KOH	13.5	95.5	320.0	6.0	Nano-Micro Lett.[1]
In_2O_3@C	1.0 M KOH	13.5	91.1	129.4	2.4	Appl. Catal. B Environ.[2]
S2-In	0.5 M $KHCO_3$	7.2	93.0	80.9	1.5	Nat. Commun.[3]
Bi-CrO_x	1.0 M KOH	13.5	96.5	687.6	12.9	Angew. Chem. Int. Ed.[4]
Cu-Bi	1.0 M KOH	13.5	93.2	209.7	3.9	Angew. Chem. Int. Ed.[5]
Bi NSs	1.0 M KOH	13.5	89.0	364.9	6.8	Adv. Energy Mater.[6]
CT/h-BiOBr	1.0 M KOH	13.5	87.0	316.0	5.9	ACS Nano[7]
$Bi_{0.1}Sn$	1.0 M KOH	13.5	93.5	138.0	2.6	Nat. Commun.[8]
nBuLi-Bi	1.0 M $KHCO_3$	8.5	92.0	460.0	8.5	Nat. Commun.[9]
BH-10	1.0 M KOH	13.5	95.7	564.9	10.6	Angew. Chem. Int. Ed.[10]
Bi-ene-NW	1.0 M KOH	13.5	92.0	515.0	9.7	Energy Environ. Sci.[11]

Supplementary Table 2. Comparison of SPCE performance between our work and those reported in the literature.

Catalyst	Electrolyte	pH	FE_{HCOOH} (%)	CO_2 flow rate (sccm)	SPCE (%)	Reference
Bi/CCNT	0.05 M H_2SO_4 + 3.0 M KCl	0.52	95.3	2	68.5	This work
Sn(S)-H	H_2SO_4 + 0.5 M K_2SO_4	3	61.5	5	34.8	Nat. Commun.[12]
SiC-Nafion^{TM}/SnBi/PTFE	0.05 M H_2SO_4 + 3.0 M KCl	1	88.6	3	65.0	Angew. Chem. Int. Ed.[13]
Bi NS	0.05 M H_2SO_4 + 3.0 M KCl	0.52	92.2	3	27.4	ACS Catal.[14]
Sn SACs	H_2SO_4 + 0.5 M K_2SO_4	3	90.8	10	13.3	Angew. Chem. Int. Ed.[15]
BiS-1	0.5 M K_2SO_4	8.5	64.1	3	47.9	Angew. Chem. Int. Ed.[16]
	0.05 M H_2SO_4 + 0.5 M K_2SO_4	2	87.5	3	65.4	
Cu_6Sn_5	0.05 M H_2SO_4 + 3.0 M KCl	1	62.1	3	77.4	Nat. Commun.[17]
SnO_2/C	0.1 M H_2SO_4+ 0.4 M K_2SO_4	1	84.4	50	4.5	Nat. Catal.[18]
2D-Bi	0.5 M $KHCO_3$	7.4	96.5	20	6.4	Nat. Energy[19]
$Bi_{0.1}Sn$	1.0 M $KHCO_3$	8	95.5	20	3.6	Nat. Commun.[8]
BiBrO	2.0 M $KHCO_3$	8.5	90.1	10	13.5	Adv. Mater.[20]
Bi-MOF-TS	0.02 M H_2SO_4 + 0.1 M K_2SO_4	1.7	62.5	1	63.2	Nat. Commun.[21]

Supplementary Table 3. The quantification of alkali cations in the electrolyte* by inductively coupled plasma (ICP) measurements.

Alkali cation	Li	Na	K**	Cs
Concentration (ppm)	0.234	0.172	3.526	0.168

*The electrolyte was taken after 130-h electrolysis.

**The trace K^+ comes from the Ag/AgCl electrode which is filled with 3.0 M KCl.

Supplementary Table 4. Comparison of the energy utilization efficiency (EUE) and partial current density of our work and latest representative works from literature measured in GDE-based devices.

Catalyst	Electrolyte	Product	$FE_{product}$ (%)	$j_{product}$ (mA cm^{-2})	EUE (%)	Reference
Bi/CCNT	0.05 M H_2SO_4 + 3.0 M $N(CN_3)_4Cl$	HCOOH	90.8	321	32.9	This work
	0.05 M H_2SO_4 + 3.0 M $N(CN_3)_4Cl$ + 0.1 M KCl		92.8	370	33.6	
Ag/CCNT	0.05 M H_2SO_4 + 3.0 M $N(CN_3)_4Cl$	CO	98.2	314	31.7	
	0.05 M H_2SO_4 + 3.0 M $N(CN_3)_4Cl$ + 0.1 M KCl		99.5	379	33.7	
CuO/CCNT	0.05 M H_2SO_4 + 3.0 M $N(CN_3)_4Cl$	C_2H_4	45.9	238	13.1	
	0.05 M H_2SO_4 + 3.0 M $N(CN_3)_4Cl$ + 0.1 M KCl		51.5	299	14.7	
Cu/ICM*	0.01 M H_2SO_4	C_2H_4	33.8	68	8.4	Nat. Synth.[22]
Ni-N-C/PTFE**	1.0 M Cs_2SO_4 + H_2SO_4 (pH=2)	CO	99.2	249	29.4	Adv. Mater.[23]
Cu/Hex-Aza-COF**	1.0 M H_3PO_4 + 1.0 M KCl	C_2H_4	30.4	152	8.9	Nat. Energy[24]
SiC-Nafion™/Cu/PTFE*	0.05 M H_2SO_4 + 3.0 M KCl	C_2H_4	40.1	40	11.8	Angew. Chem. Int. Ed.[13]
SiC-NafionTM/SnBi/PTFE*		HCOOH	82.5	83	29.1	
Ag/PDDA-GO*	0.01 M H_2SO_4	CO	55.1	165	17.8	Angew. Chem. Int. Ed.[25]
Cu/GC-medium*	0.2 M H_2SO_4	C_2H_4	40.2	80	9.2	Nat. Catal.[26]
Ni-N-C***	0.1 M K_2SO_4 + H_2SO_4 (pH=0.5)	CO	55.9	168	23.2	Energy Environ. Sci.[27]
Cu/CAL*	1.0 M H_3PO_4 + 3.0 M KCl	C_2H_4	23.5	282	6.3	Science[28]
Cu/PCRL*	0.01 M H_2SO_4	C_2H_4	34.6	35	9.5	ACS Energy Lett.[29]
Cu/PTFE/COF:PFSA*	1.0 M H_3PO_4 + 3.0 M KCl	C_2H_4	36.7	114	10.8	Nat. Synth.[30]
Ag/c-PDDA**	0.1 M H_2SO_4	CO	81.2	243	32.3	Nat. Commun.[31]
In/c-PDDA**		HCOOH	71.8	219	29.2	
In_2O_3/C***	0.05 M H_2SO_4 + 0.05 M K_2SO_4	HCOOH	94.8	285	25.4	Nat. Commun.[32]

*Polymer-coating strategy with layered structure

**Polymer-coating strategy with mixed structure

***Alkali-cation strategy with low concentration of K^+

Supplementary Table 5. Comparison of acidic CO_2 reduction reported in literatures based on (alkyl)ammonium-cation electrolytes.

Catalyst	Electrolyte	Product	pH	$FE_{product}$ (%)	$j_{product}$ (mA cm^{-2})	Stability (h)	Reference
Bi/CCNT	0.1 M H^+ + 3.0 M $N(CH_3)_4^+$	HCOOH	Acidic	90.1	378	130	This work
Ag/CCNT		CO		98.2	314	160	
CuO/CCNT		C_2H_4		45.9	238	60	
Au NPs	1.0 M $N(CH_3)_4^+$ (pH=2)	CO	Acidic	85.1	68	0.5	J. Am. Chem. Soc.[33]
CuO NPs	1.0 M $N(CH_3)_4^+$ (pH=14)	C_2H_4	Akaline	33.2	166	10	EES Catal.[34]
Ag NPs	0.1 M H^+ + 1.0 M NH_4^+	CO	Acidic	38.3	38.3	7	ACS Catal.[35]
AuPTFE	0.1 M $N(CH_3CH_2)_4^+$	CO	neutral	78.5	5.1	0.3	J. Am. Chem. Soc.[36]
Bi/C	0.1 M $N(CH_3)_4^+$	HCOOH	neutral	32.2	1.65	2	ACS Catal.[37]

Supplementary Table 6. RDE results for our CCNT-modified catalysts as measured in 0.05 M H_2SO_4 + 0.5 M K_2SO_4.

	$j_{plateau}$ (mA) vs. $\omega^{1/2}$			
Electrode	Slope (mA $s^{-1/2}$)	R^2	$Slope_{CCNT-n}/Slope_{CNT}$	$D_{obs, H+, CCNT-n}/D_{obs, H+, CNT}$
CNT	2.5307	0.9991	1.000	1.000
CCNT-0.125	2.4728	0.9994	0.977	0.986
CCNT-0.5	2.4101	0.9993	0.952	0.968
CCNT-1.0	2.3745	0.9993	0.938	0.958
CCNT-2.0	2.3357	0.9994	0.923	0.949

Supplementary Method

Rotating disk electrode experiments: The diffusion-limited current of hydronium reduction was calculated according to the Levich equation:

$$j_{plateau} = 0.62nFAD^{\frac{3}{2}}v^{-\frac{1}{6}}c_{0,H^+}\omega^{\frac{1}{2}} \quad (1)$$

where n is the number of electrons transferred in the reaction, F is the Faraday constant (9.65×10^4 C mol^{-1}), A is the electrode surface area, D is the diffusion coefficient of hydronium ions, v is the kinematic viscosity of electrolyte, c_{0,H^+} is the bulk concentration of hydronium ions, and ω is the rotation speed of the RDE (rad s^{-1}).

Then the kinetic current density can be obtained from the Koutecký-Levich equation:

$$\frac{1}{j_{tot}} = \frac{1}{j_k} + \frac{1}{j_{plateau}} \quad (2)$$

where j_{tot} is the total current density, j_k is the kinetic current density and $j_{plateau}$ is the diffusion limiting current density.

Supplementary References

1. Qiu, C. et al. MOF-transformed In_2O_{3-x}@C nanocorn electrocatalyst for efficient CO_2 reduction to HCOOH. *Nano-Micro Lett.* **14**, 167 (2022).
2. Meng, J. et al. Regulating p-orbital electronic configuration of In_2O_3 by thickness-controlled carbon layer for efficient electrocatalytic CO_2 reduction to HCOOH. *Appl. Catal. B Environ.* **361**, 124596 (2025).
3. Ma, W. et al. Promoting electrocatalytic CO_2 reduction to formate via sulfur-boosting water activation on indium surfaces. *Nat. Commun.* **10**, 892 (2019).
4. Lei, P.-X. et al. Integrated "Two-in-One" strategy for hgh-rate electrocatalytic CO_2 reduction to formate. *Angew. Chem. Int. Ed.* **64**, e202415726 (2025).
5. Li, Z. et al. Electron-rich Bi nanosheets promote $CO_2{\cdot}^-$ formation for high-performance and pH-universal electrocatalytic CO_2 reduction. *Angew. Chem. Int. Ed.* **62**, e202217569 (2023).
6. Yang, J. et al. Bi-based metal-organic framework derived leafy bismuth nanosheets for carbon dioxide electroreduction. *Adv. Energy Mater.* **10**, 2001709 (2020).
7. Chen, Y. et al. Amphipathic surfactant on reconstructed bismuth enables industrial-level electroreduction of CO_2 to formate. *ACS Nano* **18**, 19345-19353 (2024).
8. Li, L. et al. Stable, active CO_2 reduction to formate via redox-modulated stabilization of active sites. *Nat. Commun.* **12**, 5223 (2021).
9. Fan, L., Xia, C., Zhu, P., Lu, Y. & Wang, H. Electrochemical CO_2 reduction to high-concentration pure formic acid solutions in an all-solid-state reactor. *Nat. Commun.* **11**, 3633 (2020).
10. Li, Y. et al. Enhancing local CO_2 adsorption by L-histidine incorporation for selective formate production over the wide potential window. *Angew. Chem. Int. Ed.* **62**, e202313522 (2023).
11. Zhang, M. et al. Engineering a conductive network of atomically thin bismuthene with rich defects enables CO_2 reduction to formate with industry-compatible current densities and stability. *Energy Environ. Sci.* **14**, 4998-5008 (2021).
12. Shen, H. et al. Acidic CO_2-to-HCOOH electrolysis with industrial-level current on phase engineered tin sulfide. *Nat. Commun.* **14**, 2843 (2023).
13. Li, L., Liu, Z., Yu, X. & Zhong, M. Achieving high single-pass carbon conversion efficiencies in durable CO_2 electroreduction in strong acids via electrode structure engineering. *Angew. Chem. Int. Ed.* **62**, e202300226 (2023).
14. Qiao, Y. et al. Engineering the local microenvironment over Bi nanosheets for highly selective electrocatalytic conversion of CO_2 to HCOOH in strong acid. *ACS Catal.* **12**, 2357-2364 (2022).
15. Sun, B. et al. Unveiling pH-dependent adsorption strength of $^*CO_2^-$ intermediate over high-density Sn single atom catalyst for acidic CO_2-to-HCOOH electroreduction. *Angew. Chem. Int. Ed.* **63**, e202318874 (2024).
16. Jiang, Z. et al. pH-universal electrocatalytic CO_2 reduction with ampere-level current density on doping-engineered bismuth sulfide. *Angew. Chem. Int. Ed.* **63**, e202408412 (2024).
17. Yu, X. et al. Coverage enhancement accelerates acidic CO_2 electrolysis at ampere-level current

with high energy and carbon efficiencies. *Nat. Commun.* **15**, 1711 (2024).

18. Gu, J., Liu, S., Ni, W., Ren, W., Haussener, S. & Hu, X. Modulating electric field distribution by alkali cations for CO_2 electroreduction in strongly acidic medium. *Nat. Catal.* **5**, 268-276 (2022).

19. Xia, C. et al. Continuous production of pure liquid fuel solution via electrocatalytic CO_2 reduction using solid-electrolyte devices. *Nat. Energy* **4**, 776-785 (2019).

20. García de Arquer, F. P. *et al.* 2D metal oxyhalide-derived catalysts for efficient CO_2 electroreduction. *Adv. Mater.* **30**, 1802858 (2018).

21. Chen, X. et al. Activating inert non-defect sites in Bi catalysts using tensile strain engineering for highly active CO_2 electroreduction. *Nat. Commun.* **16**, 1927 (2025).

22. Shayesteh Zeraati, A. et al. Carbon- and energy-efficient ethanol electrosynthesis via interfacial cation enrichment. *Nat. Synth.* **4**, 75-83 (2025).

23. Sheng, X., Ge, W., Jiang, H. & Li, C. Engineering the Ni-N-C catalyst microenvironment enabling CO_2 electroreduction with nearly 100% CO selectivity in acid. *Adv. Mater.* **34**, 2201295 (2022).

24. Ozden, A. et al. Energy- and carbon-efficient CO_2/CO electrolysis to multicarbon products via asymmetric ion migration–adsorption. *Nat. Energy* **8**, 179-190 (2023).

25. Fan, J. et al. Immobilized tetraalkylammonium cations enable metal-free CO_2 electroreduction in acid and pure water. *Angew. Chem. Int. Ed.* **63**, e202317828 (2024).

26. Fan, M. et al. Cationic-group-functionalized electrocatalysts enable stable acidic CO_2 electrolysis. *Nat. Catal.* **6**, 763-772 (2023).

27. Li, H. et al. Tailoring acidic microenvironments for carbon-efficient CO_2 electrolysis over a Ni-N-C catalyst in a membrane electrode assembly electrolyzer. *Energy Environ. Sci.* **16**, 1502-1510 (2023).

28. Huang, J. E. et al. CO_2 electrolysis to multicarbon products in strong acid. *Science* **372**, 1074-1078 (2021).

29. O'Brien, C. P. et al. Single pass CO_2 conversion exceeding 85% in the electrosynthesis of multicarbon products via local CO_2 regeneration. *ACS Energy Lett.* **6**, 2952-2959 (2021).

30. Zhao, Y. et al. Conversion of CO_2 to multicarbon products in strong acid by controlling the catalyst microenvironment. *Nat. Synth.* **2**, 403-412 (2023).

31. Qin, H. G. et al. Surface-immobilized cross-linked cationic polyelectrolyte enables CO_2 reduction with metal cation-free acidic electrolyte. *Nat. Commun.* **14**, 5640 (2023).

32. Wang, Z. et al. Tip carbon encapsulation customizes cationic ebrichment and valence stabilization for low K^+ acidic CO_2 electroreduction. *Nat. Commun.* **16**, 1754 (2025).

33. Shi, K. *et al.* Ammonium cation-promoted CO_2 electroreduction on Au in acidic media. *J. Am. Chem. Soc.* **147**, 23277-23285 (2025).

34. Kurihara, R., Ito, S., Kato, S., Harada, T., Nakanishi, S. & Kamiya, K. Alkali-cation-free electrochemical CO_2 reduction to multicarbon products in aqueous electrolytes containing tetraalkylammonium cations. *EES Catal.* **3**, 1055-1061 (2025).

35. Peng, C. *et al.* Ultradiluted (alkyl)ammonium enables acidic CO_2 electroreduction. *ACS Catal.* **15**, 13346-13352 (2025).

36. Weng, S., Toh, W. L. & Surendranath, Y. Weakly coordinating organic cations are intrinsically capable of supporting CO_2 reduction catalysis. *J. Am. Chem. Soc.* **145**, 16787-16795 (2023).

37. Shi, K., Le, D., Panagiotakopoulos, T., Rahman, T. S. & Feng, X. Effect of ammonium-based cations on CO_2 electroreduction. *ACS Catal.* **15**, 3647-3659 (2025).